

1 SEARCH FOR PRODUCTION OF A HIGGS BOSON AND A SINGLE TOP  
2 QUARK IN MULTILEPTON FINAL STATES IN  $pp$  COLLISIONS AT  $\sqrt{s} = 13$   
3 TeV.

4 by

5 Jose Andres Monroy Montañez

6 A DISSERTATION

7 Presented to the Faculty of

8 The Graduate College at the University of Nebraska

In Partial Fulfilment of Requirements

10 For the Degree of Doctor of Philosophy

11 Major: Physics and Astronomy

12 Under the Supervision of Kenneth Bloom and Aaron Dominguez

13 Lincoln, Nebraska

14 July, 2018

15 SEARCH FOR PRODUCTION OF A HIGGS BOSON AND A SINGLE TOP  
16 QUARK IN MULTILEPTON FINAL STATES IN pp COLLISIONS AT  $\sqrt{s} = 13$   
17 TeV.

18 Jose Andres Monroy Montañez, Ph.D.

19 University of Nebraska, 2018

20 Adviser: Kenneth Bloom and Aaron Dominguez

# **<sup>21</sup> Table of Contents**

<b><sup>22</sup> Table of Contents</b>	<b>iii</b>
<b><sup>23</sup> List of Figures</b>	<b>v</b>
<b><sup>24</sup> List of Tables</b>	<b>vii</b>
<b><sup>25</sup> 1 INTRODUCTION</b>	<b>1</b>
<b><sup>26</sup> 2 Theoretical approach</b>	<b>2</b>
27     2.1 Introduction . . . . .	2
28     2.2 Standard model of particle physics . . . . .	3
29     2.2.1 Fermions . . . . .	5
30     2.2.1.1 Leptons . . . . .	6
31     2.2.1.2 Quarks . . . . .	8
32     2.2.2 Fundamental interactions . . . . .	12
33     2.2.3 Gauge bosons . . . . .	18
34     2.3 Electroweak unification and the Higgs mechanism . . . . .	20
35     2.3.1 Spontaneous symmetry breaking (SSB) . . . . .	28
36     2.3.2 Higgs mechanism . . . . .	32
37     2.3.3 Masses of the gauge bosons . . . . .	34

38	2.3.4	Masses of the fermions . . . . .	35
39	2.3.5	The Higgs field . . . . .	36
40	2.3.6	Production of Higgs bosons at LHC . . . . .	37
41	2.3.7	Higgs boson decay channels . . . . .	41
42	2.4	Associated production of a Higgs boson and a single Top quark. . . . .	42
43	2.5	The CP-mixing in tH processes . . . . .	47
44	2.6	Experimantal status of the anomalous Higg-fermion coupling. . . . .	51
45	<b>3</b>	<b>The CMS experiment at the LHC</b>	<b>53</b>
46	3.1	Introduction . . . . .	53
47	3.2	The LHC . . . . .	54
48	3.3	The CMS experiment . . . . .	63
49	3.3.1	Coordinate system . . . . .	65
50	3.3.2	Pixels detector . . . . .	67
51	3.3.3	Silicon strip tracker . . . . .	69
52	3.3.4	Electromagnetic calorimeter . . . . .	70
53	3.3.5	Hadronic calorimeter . . . . .	72
54	3.3.6	Superconducting solenoid magnet . . . . .	73
55	3.3.7	Muon system . . . . .	75
56	3.3.8	CMS trigger system . . . . .	76
57	3.3.9	CMS computing . . . . .	78
58	<b>Bibliography</b>		<b>80</b>
59	<b>References</b>		<b>82</b>

# <sup>60</sup> List of Figures

61	2.1 Standard model of particle physics. . . . .	4
62	2.2 Transformations between quarks . . . . .	12
63	2.3 Fundamental interactions in nature. . . . .	13
64	2.4 SM interactions diagrams . . . . .	14
65	2.5 Neutral current processes . . . . .	21
66	2.6 Spontaneous symmetry breaking mechanism . . . . .	28
67	2.7 SSB Potential form . . . . .	29
68	2.8 Potential for complex scalar field . . . . .	30
69	2.9 SSB mechanism for complex scalar field . . . . .	31
70	2.10 Proton-Proton collision . . . . .	38
71	2.11 Higgs boson production mechanism Feynman diagrams . . . . .	39
72	2.12 Higgs boson production cross section and decay branching ratios . . . . .	40
73	2.13 Associated Higgs boson production mechanism Feynman diagrams . . . . .	43
74	2.14 Cross section for tHq process as a function of $\kappa_t$ . . . . .	45
75	2.15 Cross section for $tHW$ process as a function of $\kappa_{Htt}$ . . . . .	46
76	2.16 NLO cross section for $tX_0$ and $t\bar{t}X_0$ . . . . .	49
77	2.17 NLO cross section for $tWX_0$ , $t\bar{t}X_0$ . . . . .	50

78	2.18 Two dimentional $\kappa_t$ - $\kappa_V$ plot of the coupling modifiers. ATLAS and CMS 79 combination. . . . .	51
80	3.1 CERN accelerator complex . . . . .	54
81	3.2 LHC protons source. First acceleration stage. . . . .	55
82	3.3 The LINAC2 accelerating system at CERN. . . . .	56
83	3.4 LHC layout and RF cavities module. . . . .	57
84	3.5 LHC dipole magnet. . . . .	59
85	3.6 Integrated luminosity delivered by LHC and recorded by CMS during 2016	61
86	3.7 LHC interaction points . . . . .	62
87	3.8 Multiple pp collision bunch crossing at CMS. . . . .	64
88	3.9 Layout of the CMS detector . . . . .	65
89	3.10 CMS detector coordinate system . . . . .	66
90	3.11 CMS pixel detector schematic view. . . . .	68
91	3.12 SST Schematic view. . . . .	69
92	3.13 CMS ECAL schematic view . . . . .	71
93	3.14 CMS HCAL schematic view . . . . .	72
94	3.15 CMS solenoid magnet . . . . .	74
95	3.16 CMS Muon system schematic view . . . . .	75
96	3.17 CMS Level-1 trigger architecture . . . . .	77
97	3.18 WLCG structure . . . . .	78
98	3.19 Data flow from CMS detector through hardware Tiers . . . . .	81

## <sup>99</sup> List of Tables

100	2.1	Fermions of the SM. . . . .	5
101	2.2	Fermion masses. . . . .	6
102	2.3	Leptons properties. . . . .	9
103	2.4	Quarks properties. . . . .	9
104	2.5	Fermion weak isospin and weak hypercharge multiplets. . . . .	11
105	2.6	Fundamental interactions features. . . . .	15
106	2.7	SM gauge bosons. . . . .	19
107	2.8	Higgs boson properties. . . . .	37
108	2.9	Predicted branching ratios for a SM Higgs boson with $m_H = 125 \text{ GeV}/c^2$ . . . . .	42
109	2.10	Predicted SM cross sections for $tH$ production at $\sqrt{s} = 13 \text{ TeV}$ . . . . .	44
110	2.11	Predicted enhancement of the $tHq$ and $tHW$ cross sections at LHC . . . . .	47

<sup>111</sup> Chapter 1

<sup>112</sup> INTRODUCTION

<sup>113</sup> **Chapter 2**

<sup>114</sup> **Theoretical approach**

<sup>115</sup> **2.1 Introduction**

<sup>116</sup> The physical description of the universe is a challenge that physicists have faced by  
<sup>117</sup> making theories that refine existing principles and proposing new ones in an attempt  
<sup>118</sup> to embrace emerging facts and phenomena.

<sup>119</sup>

<sup>120</sup> At the end of 1940s Julian Schwinger [1] and Richard P. Feynman [2], based in the  
<sup>121</sup> work of Sin-Itiro Tomonaga [3], developed an electromagnetic theory consistent with  
<sup>122</sup> special relativity and quantum mechanics that describes how matter and light inter-  
<sup>123</sup> act; the so-called “quantum eletrodynamics” (QED) had born.

<sup>124</sup>

<sup>125</sup> QED has become the guide in the development of theories that describe the universe.  
<sup>126</sup> It was the first example of a quantum field theory (QFT), which is the theoretical  
<sup>127</sup> framework for building quantum mechanical models that describes particles and their  
<sup>128</sup> interactions. QFT is composed of a set of mathematical tools that combines classical  
<sup>129</sup> fields, special relativity and quantum mechanics, while keeping the quantum point

130 particles and locality ideas.

131 This chapter gives an overview of the standard model of particle physics, starting  
 132 with a description of the particles and interactions that compose it, followed by a  
 133 description of the electroweak interaction, the Higgs boson and the associated pro-  
 134 duction of Higgs boson and a single top quark ( $tH$ ). The description contained in  
 135 this chapter is based on references [4–6].

## 136 2.2 Standard model of particle physics

137 Particle physics at the fundamental level is modeled in terms of a collection of in-  
 138 teracting particles and fields in a theory known as the “standard model of particle  
 139 physics (SM)”<sup>1</sup>.

140

141 The full picture of the SM is composed of three fields<sup>2</sup>, whose excitations are inter-  
 142 preted as particles called mediators or force-carriers; a set of fields, whose excitations  
 143 are interpreted as elementary particles, interacting through the exchange of those  
 144 mediators and a field that gives the mass to elementary particles. Figure 2.1 shows  
 145 an scheme of the SM particles organization. In addition to the particles in the scheme  
 146 (but not listed in it), their corresponding anti-particles, with opposite quantum num-  
 147 bers, are also part of the picture; some particles are their own anti-particles, like  
 148 photon or Higgs, or anti-particle is already listed like in the  $W^+$  and  $W^-$  case.

149

150 The mathematical formulation of the SM is based on group theory and the use of  
 151 Noether’s theorem [8] which states that for a physical system modeled by a Lagrangian

---

<sup>1</sup> The formal and complete treatment of the SM is out of the scope of this document, however a plenty of textbooks describing it at several levels are available in the literature. The treatment in references [?] is quite comprehensive and detailed.

<sup>2</sup> Note that gravitational field is not included in the standard model formulation

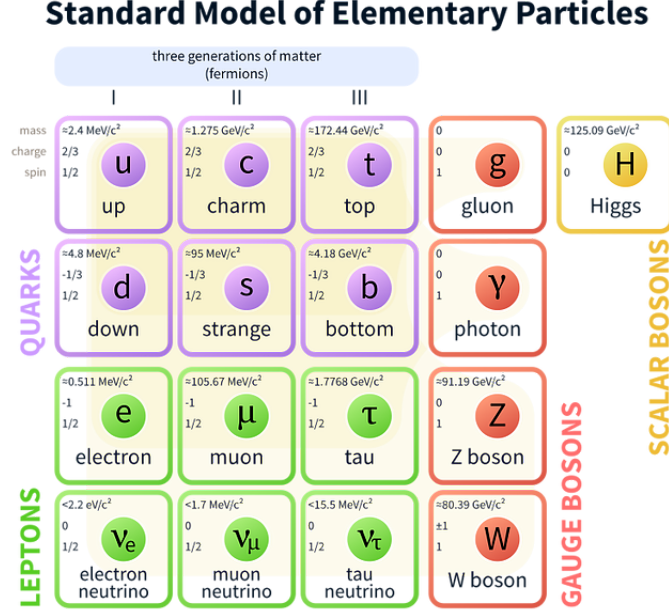


**Figure 2.1:** Schematic representation of the Standard model of particle physics. SM is a theoretical model intended to describe three of the four fundamental forces of the universe in terms of a set of particles and their interactions. [7].

152 that is invariant under a group of transformations a conservation law is expected. For  
 153 instance, a system described by a time-independent Lagrangian is invariant (symmet-  
 154 ric) under time changes (transformations) with the total energy conservation law as  
 155 the expected conservation law. In QED, the charge operator ( $Q$ ) is the generator of  
 156 the  $U(1)$  symmetry which according to the Noether's theorem means that there is a  
 157 conserved quantity; this conserved quantity is the electric charge and thus the law  
 158 conservation of electric charge is established.

159

160 In the SM, the symmetry group  $SU(3)_C \otimes SU(2)_L \otimes U(1)_Y$  describes three of the  
 161 four fundamental interactions in nature(see section 2.2.2): strong interaction(SI),  
 162 weak interaction(WI) and electromagnetic interactions (EI) in terms of symmetries  
 163 associated to physical quantities:

- 164     • Strong:  $SU(3)_C$  associated to color charge
- 165     • Weak:  $SU(2)_L$  associated to weak isospin and chirality
- 166     • Electromagnetic:  $U(1)_Y$  associated to weak hypercharge and electric charge
- 167     It will be shown that the electromagnetic and weak interactions are combined in  
 168     the so-called electroweak interaction where chirality, hypercharge, weak isospin and  
 169     electric charge are the central concepts.

170 **2.2.1 Fermions**

171     The basic constituents of the ordinary matter at the lowest level, which form the set  
 172     of elementary particles in the SM formulation, are quarks and leptons. All of them  
 173     have spin 1/2, therefore they are classified as fermions since they obey Fermi-Dirac  
 174     statistics. There are six “flavors” of quarks and three of leptons organized in three  
 175     generations, or families, as shown in table 2.1.

176

		Generation		
		1st	2nd	3rd
Leptons	Charged	Electron (e)	Moun( $\mu$ )	Tau ( $\tau$ )
	Neutral	Electron neutrino ( $\nu_e$ )	Muon neutrino ( $\nu_\mu$ )	Tau neutrino ( $\nu_\tau$ )
Quarks	Up-type	Up (u)	Charm (c)	Top (t)
	Down-type	Down (d)	Strange (s)	Bottom (b)

**Table 2.1:** Fermions of the SM. There are six flavors of quarks and three of leptons, organized in three generations, or families, composed of two pairs of closely related particles. The close relationship is motivated by the fact that WI between leptons is limited to the members of the same generation; WI between quarks is not limited but greatly favoured, to same generation members.

177

178     There is a mass hierarchy between generations (see table 2.2), where the higher gener-  
 179     ation particles decays to the lower one, which can explain why the ordinary matter is

made of particles in the first generation. In the SM, neutrinos are modeled as massless particles so they are not subject to this mass hierarchy; however, today it is known that neutrinos are massive so the hierarchy could be restated. The reason behind this mass hierarchy is one of the most important open questions in particle physics, and it becomes more puzzling when noticing that the mass difference between first and second generation fermions is small compared to the mass difference with respect to the third generation.

Lepton	Mass (MeV/c <sup>2</sup> )	Quark	Mass (MeV/c <sup>2</sup> )
e	0.51	u	2.2
$\mu$	105.65	c	$1.28 \times 10^3$
$\tau$	1776.86	t	$173.1 \times 10^3$
$\nu_e$	Unknown	d	4.7
$\nu_\mu$	Unknown	s	96
$\tau_\mu$	Unknown	b	$4.18 \times 10^3$

**Table 2.2:** Fermion masses [9]. Generations differ by mass in a way that have been interpreted as a masss hierarchy. Approximate values with no uncertainties are used, for comparison purpose.

187

Usually, the second and third generation fermions are produced in high energy processes, like the ones recreated in particle accelerators.

### 190 2.2.1.1 Leptons

A lepton is an elementary particle that is not subject to the SI. As seen in table 2.1, there are two types of leptons, the charged ones (electron, muon and tau) and the neutral ones (the three neutrinos). The electric charge (Q) is the property that gives leptons the ability to participate in the EI. From the classical point of view, Q plays a central role determining, among others, the strength of the electric field through which the electromagnetic force is exerted. It is clear that neutrinos are not affected

197 by EI because they don't carry electric charge.

198

199 Another feature of the leptons that is fundamental in the mathematical description  
 200 of the SM is the chirality, which is closely related to spin and helicity. Helicity defines  
 201 the handedness of a particle by relating its spin and momentum such that if they  
 202 are parallel then the particle is right-handed; if spin and momentum are antiparallel  
 203 the particle is said to be left-handed. The study of parity conservation (or viola-  
 204 tion) in  $\beta$ -decay has shown that only left-handed electrons/neutrinos or right-handed  
 205 positrons/anti-neutrinos are created [10]; the inclusion of that feature in the theory  
 206 was achieved by using projection operators for helicity, however, helicity is frame de-  
 207 pendent for massive particles which makes it not Lorentz invariant and then another  
 208 related attribute has to be used: *chirality*.

209

210 Chirality is a purely quantum attribute which makes it not so easy to describe in  
 211 graphical terms but it defines how the wave function of a particle transforms under  
 212 certain rotations. As with helicity, there are two chiral states, left-handed chiral (L)  
 213 and right-handed chiral (R). In the highly relativistic limit where  $E \approx p \gg m$  helicity  
 214 and chirality converge, becoming exactly the same for massless particles.

215

216 In the following, when referring to left-handed (right-handed) it will mean left-handed  
 217 chiral (right-handed chiral). The fundamental fact about chirality is that while EI  
 218 and SI are not sensitive to chirality, in WI left-handed and right-handed fermions are  
 219 treated asymmetrically, such that only left handed fermions and right-handed anti-  
 220 fermions are allowed to couple to WI mediators, which is a violation of parity. The  
 221 way to translate this statement in a formal mathematical formulation is based on the  
 222 isospin symmetry group  $SU(2)_L$ .

223

224 Each generation of leptons is seen as a weak isospin doublet.<sup>3</sup> The left-handed charged  
 225 lepton and its associated left-handed neutrino are arranged in doublets of weak isospin  
 226 T=1/2 while their right-handed partners are singlets:

$$\begin{pmatrix} \nu_l \\ l \end{pmatrix}_L, l_R := \begin{pmatrix} \nu_e \\ e \end{pmatrix}_L, \begin{pmatrix} \nu_\mu \\ \mu \end{pmatrix}_L, \begin{pmatrix} \nu_\tau \\ \tau \end{pmatrix}_L, e_R, \mu_R, \tau_R, \nu_{eR}, \nu_{\mu R}, \nu_{\tau R} \quad (2.1)$$

227 The isospin third component refers to the eigenvalues of the weak isospin operator  
 228 which for doublets is  $T_3 = \pm 1/2$ , while for singlets it is  $T_3 = 0$ . The physical meaning  
 229 of this doublet-singlet arrangement falls in that the WI couples the two particles in  
 230 the doublet by exchanging the interaction mediator while the singlet member is not  
 231 involved in WI. The main properties of the leptons are summarized in table 2.3.

232

233 Altough all three flavor neutrinos have been observed, their masses remain unknown  
 234 and only some estimations have been made [11]. The main reason is that the fla-  
 235 vor eigenstates are not the same as the mass eigenstates which implies that when  
 236 a neutrino is created its mass state is a linear combination of the three mass eigen-  
 237 states and experiments can only probe the squared difference of the masses. The  
 238 Pontecorvo-Maki-Nakagawa-Sakata (PMNS) mixing matrix encode the relationship  
 239 between flavor and mass eigenstates.

240

### 241 2.2.1.2 Quarks

242 Quarks are the basic constituents of protons and neutrons. The way quarks join to  
 243 form bound states, called “hadrons”, is through the SI. Quarks are affected by all the

---

<sup>3</sup> The weak isospin is an analogy of the isospin symmetry in strong interaction where neutron and proton are affected equally by strong force but differ in their charge.

Lepton	Q(e)	$T_3$	$L_e$	$L_\mu$	$L_\tau$	Lifetime (s)
Electron (e)	-1	-1/2	1	0	0	Stable
Electron neutrino( $\nu_e$ )	0	1/2	1	0	0	Unknown
Muon ( $\mu$ )	-1	-1/2	0	1	0	$2.19 \times 10^{-6}$
Muon neutrino ( $\nu_\mu$ )	0	1/2	0	1	0	Unknown
Tau ( $\tau$ )	-1	-1/2	0	0	1	$290.3 \times 10^{-15}$
Tau neutrino ( $\tau_\mu$ )	0	1/2	0	0	1	Unknown

**Table 2.3:** Leptons properties [9]. Q: electric charge,  $T_3$ : weak isospin. Only left-handed leptons and right-handed anti-leptons participate in the WI. Anti-particles with inverted  $T_3$ , Q and lepton number complete the leptons set but are not listed. Right-handed leptons and left-handed anti-leptons, neither listed, form weak isospin singlets with  $T_3 = 0$  and do not take part in the weak interaction.

244 fundamental interactions which means that they carry all the four types of charges:  
 245 color, electric charge, weak isospin and mass.

Flavor	Q(e)	$I_3$	$T_3$	B	C	S	T	$B'$	Y	Color
Up (u)	2/3	1/2	1/2	1/3	0	0	0	0	1/3	r,b,g
Charm (c)	2/3	0	1/2	1/3	1	0	0	0	4/3	r,b,g
Top(t)	2/3	0	1/2	1/3	0	0	1	0	4/3	r,b,g
Down(d)	-1/3	-1/2	-1/2	1/3	0	0	0	0	1/3	r,b,g
Strange(s)	-1/3	0	-1/2	1/3	0	-1	0	0	-2/3	r,b,g
Bottom(b)	-1/3	0	-1/2	1/3	0	0	0	-1	-2/3	r,b,g

**Table 2.4:** Quarks properties [9]. Q: electric charge,  $I_3$ : isospin,  $T_3$ : weak isospin, B: baryon number, C: charmness, S: strangeness, T: topness,  $B'$ : bottomness, Y: hypercharge. Anti-quarks posses the same mass and spin as quarks but all charges (color, flavor numbers) have opposite sign.

246  
 247 Table 2.4 summarizes the features of quarks, among which the most particular is  
 248 their fractional electric charge. Note that fractional charge is not a problem, given  
 249 that quarks are not found isolated, but serves to explain how composed particles are  
 250 formed out of two or more valence quarks<sup>4</sup>.

251

---

<sup>4</sup> Hadrons can contain an indefinite number of virtual quarks and gluons, known as the quark and gluon sea, but only the valence quarks determine hadrons' quantum numbers.

252 Color charge is the responsible for the SI between quarks and is the symmetry  
 253 ( $SU(3)_C$ ) that defines the formalism to describe SI. There are three colors: red (r),  
 254 blue(b) and green(g) and their corresponding three anti-colors; thus each quark carries  
 255 one color unit while anti-quarks carries one anti-color unit. As said above, quarks are  
 256 not allowed to be isolated due to the color confinement effect, therefore their features  
 257 have been studied indirectly by observing their bound states created when:

- 258     • one quark with a color charge is attracted by an anti-quark with the correspond-  
 259         ing anti-color charge forming a colorless particle called a “meson.”
- 260     • three quarks (anti-quarks) with different color (anti-color) charges are attracted  
 261         among them forming a colorless particle called a “baryon(anti-baryon).”

262 In the first version of the quark model (1964), M. Gell-Mann [12] and G. Zweig  
 263 [13, 14] developed a consistent way to classify hadrons according to their properties.  
 264 Only three quarks (u, d, s) were involved in a scheme in which all baryons have  
 265 baryon number  $B=1$  and therefore quarks have  $B=1/3$ ; non-baryons have  $B=0$ . The  
 266 scheme organizes baryons in a two-dimensional space ( $I_3 - Y$ );  $Y$  (hypercharge) and  $I_3$   
 267 (isospin) are quantum numbers related by the Gell-Mann-Nishijima formula [15, 16]:

$$Q = I_3 + \frac{Y}{2} \quad (2.2)$$

268 where  $Y = B + S + C + T + B'$  are the quantum numbers listed in table 2.4. Baryon  
 269 number is conserved in SI and EI which means that single quarks cannot be created  
 270 but in pairs  $q - \bar{q}$ .

271

272 There are six quark flavors organized in three generations (see table 2.1) following a  
 273 mass hierarchy which, again, implies that higher generations decay to first generation

274 quarks.

	Quarks			$T_3$	$Y_W$	Leptons			$T_3$	$Y_W$
Doublets	$(\frac{u}{d'})_L$	$(\frac{c}{s'})_L$	$(\frac{t}{b'})_L$	$(\frac{1/2}{-1/2})$	1/3	$(\nu_e)_L$	$(\nu_\mu)_L$	$(\nu_\tau)_L$	$(\frac{1/2}{-1/2})$	-1
Singlets	$u_R$	$c_R$	$t_R$	0	4/3	$\nu_{eR}$	$\nu_{\mu R}$	$\nu_{\tau R}$	0	-2

**Table 2.5:** Fermion weak isospin and weak hypercharge multiplets. Weak hypercharge is calculated through the Gell-Mann-Nishijima formula 2.2 but using the weak isospin and charge for quarks.

275

276 Isospin doublets of quarks are also defined (see table 2.5) and as for neutrinos, the  
 277 mass eigenstates are not the same as the WI eigenstates which means that members of  
 278 different quark generations are connected by the WI mediator; thus, up-type quarks  
 279 are coupled not to down-type quarks directly but to a superposition of down-type  
 280 quarks ( $q'_d$ ) via WI according to:

$$q'_d = V_{CKM} q_d$$

281

$$\begin{pmatrix} d' \\ s' \\ b' \end{pmatrix} = \begin{pmatrix} V_{ud} & V_{us} & V_{ub} \\ V_{cd} & V_{cs} & V_{cb} \\ V_{td} & V_{ts} & V_{tb} \end{pmatrix} \begin{pmatrix} d \\ s \\ b \end{pmatrix} \quad (2.3)$$

282 where  $V_{CKM}$  is known as Cabibbo-Kobayashi-Maskawa (CKM) mixing matrix [17,18].  
 283 The weak decays of quarks are represented in the diagram of figure 2.2; again the  
 284 CKM matrix plays a central role since it contains the probabilities for the different  
 285 quark decay channels, in particular, note that quark decays are greatly favored be-  
 286 tween generation members.

287

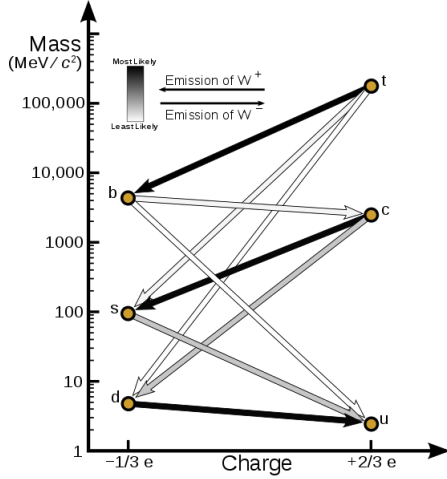


**Figure 2.2:** Transformations between quarks through the exchange of a WI. Higher generations quarks decay to first generation quarks by emitting a W boson. The arrow color indicates the likelihood of the transition according to the grey scale in the top left side which represent the CKM matrix parameters [19].

288 CKM matrix is a  $3 \times 3$  unitary matrix parametrized by three mixing angles and  
 289 the *CP-mixing phase*; the latter is the parameter responsible for the Charge-Parity  
 290 symmetry violation (CP-violation) in the SM. The fact that the b quark decays almost  
 291 all the times to a top quark is exploited in this thesis when making the selection of  
 292 the signal events by requiring the presence of a jet tagged as a jet coming from a  
 293 b quark in the final state. The effect of the *CP-mixing phase* on the cross section of  
 294 associated production of Higgs boson and a single top process is also explored in this  
 295 thesis.

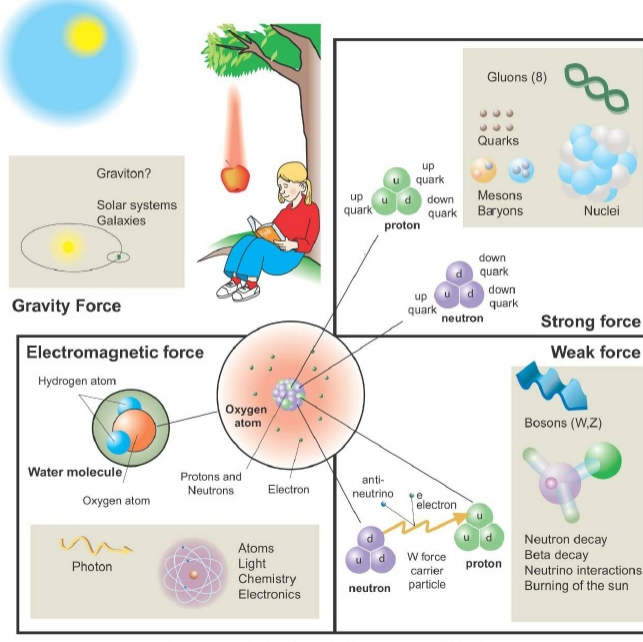
## 296 2.2.2 Fundamental interactions

297 Even though there are many manifestations of force in nature, like the ones repre-  
 298 sented in figure 2.3, we can classify all of them into one of four fundamental interac-  
 299 tions:

- 300 • *Electromagnetic interaction (EI)* affects particles that are “electrically charged,”

## Fundamental interactions.

Illustration: Typoform



Summer School KPI 15 August 2009

**Figure 2.3:** Fundamental interactions in nature. Despite the many manifestations of forces in nature, we can track all of them back to one of the fundamental interactions. The most common forces are gravity and electromagnetic given that all of us are subject and experience them in everyday life.

301 like electrons and protons. It is described by QED combining quantum mechan-  
 302 ics, special relativity and electromagnetism in order to explain how particles  
 303 with electric charge interact through the exchange of photons, therefore, one  
 304 says that “Electromagnetic Force” is mediated by “photons”. Figure 2.4a. shows  
 305 a graphical representation, known as “feynman diagram”, of electron-electron  
 306 scattering.

- 307 • *Strong interaction (SI)* described by Quantum Chromodynamics (QCD). Hadrons  
 308 like proton and neutron have internal structure given that they are composed  
 309 of two or more valence quarks<sup>5</sup>. Quarks have fractional electric charge which  
 310 means that they are subject to electromagnetic interaction and in the case of the

<sup>5</sup> particles made of four and five quarks are exotic states not so common.

311 proton they should break apart due to electrostatic repulsion; however, quarks  
 312 are held together inside the hadrons against their electrostatic repulsion by the  
 313 “Strong Force” through the exchange of “gluons.” The analog to the electric  
 314 charge is the “color charge”. Electrons and photons are elementary particles  
 315 as quarks but they don’t carry color charge, therefore they are not subject to  
 316 SI. The feynman diagram for gluon exchange between quarks is shown in figure  
 317 2.4b.

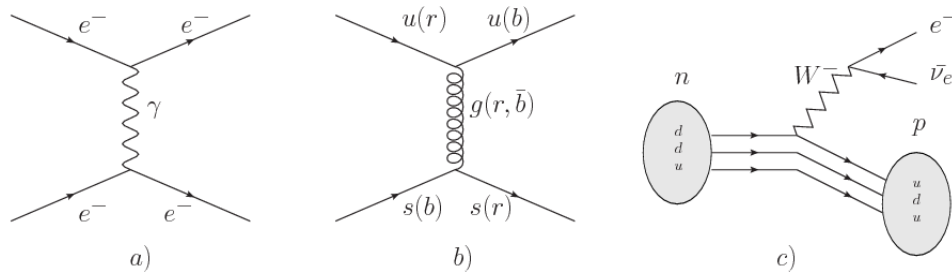


**Figure 2.4:** Feynman diagrams representing the interactions in SM; a) EI:  $e^-e^-$  scattering; b) SI: gluon exchange between quarks ; c) WI:  $\beta$ -decay

318     • *Weak interaction (WI)* described by the weak theory (WT), is responsible, for  
 319 instance, for the radioactive decay in atoms and proton-proton (pp) fusion  
 320 within the sun. Quarks and leptons are the particles affected by the weak  
 321 interaction; they possess a property called “flavor charge” (see 2.2.1) which can  
 322 be changed by emitting or absorbing one weak force mediator. There are three  
 323 mediators of the “weak force” known as “Z” boson in the case of electrically  
 324 neutral changes and “ $W^\pm$ ” bosons in the case of electrically charged changes.  
 325 The “weak isospin” is the WI analog to electric charge in EI, and color charge  
 326 in SI, and defines how quarks and leptons are affected by the weak force. Figure  
 327 2.4c. shows the feynman diagram of  $\beta$ -decay where a newtron (n) is transformed  
 328 in a proton (p) by emmiting a  $W^-$  particle. Since this thesis is in the frame  
 329 of the electroweak interaction, a more detailed description of it will be given in

330 section 2.3

- 331 • *Gravitational interaction (GI)* described by General Theory of Relativity (GR).  
 332 It is responsible for the structure of galaxies and black holes as well as the  
 333 expansion of the universe. As a classical theory, in the sense that it can be for-  
 334 mulated without even appeal to the concept of quantization, it implies that the  
 335 spacetime is a continuum and predictions can be made without limitation to the  
 336 precision of the measurement tools. The latter represent a direct contradiction  
 337 of the quantum mechanics principles. Gravity is deterministic while quantum  
 338 mechanics is probabilistic; despite that, efforts to develop a quantum theory of  
 339 gravity have predicted the “graviton” as mediator of the Gravitational force<sup>6</sup>.

Interaction	Acts on	Relative strength	Range (m)	Mediators
Electromagnetic (QED)	Electrically charged particles	$10^{-2}$	Infinite	Photon
Strong (QCD)	Quarks and gluons	1	$10^{-15}$	Gluon
Weak (WI)	Leptons and quarks	$10^{-6}$	$10^{-18}$	$W^\pm, Z$
Gravitational (GI)	Massive particles	$10^{-39}$	Infinite	Graviton

**Table 2.6:** Fundamental interactions features [20].

340

341 Table 2.6 summarizes the main features of the fundamental interactions. The rela-  
 342 tive strength of the fundamental forces reveals the meaning of strong and weak; in  
 343 a context where the relative strength of the SI is 1, the EI is about hundred times  
 344 weaker and WI is about million times weaker than the SI. A good description on  
 345 how the relative strength and range of the fundamental interactions are calculated  
 346 can be found in references [20, 21]. In the everyday life, only EI and GI are explicitly  
 347 experienced due to the range of these interactions; i.e., at the human scale distances

---

<sup>6</sup> Actually a wide variety of theories have been developed in an attempt to describe gravity; some famous examples are string theory and supergravity.

348 only EI and GI have appreciable effects, in contrast to SI which at distances greater  
 349 than  $10^{-15}$ m become negligible.

350

351 QED was built successfully on the basis of the classical electrodynamics theory (CED)  
 352 of Maxwell and Lorentz, following theoretical and experimental requirements imposed  
 353 by

- 354     • lorentz invariance: independence on the reference frame.
- 355     • locallity: interacting fields are evaluated at the same space-time point to avoid  
       356       action at a distance.
- 357     • renormalizability: physical predictions are finite and well defined
- 358     • particle spectrum, symmetries and conservation laws already known must emerge  
       359       from the theory.
- 360     • gauge invariance.

361 The gauge invariance requirement reflects the fact that the fundamental fields cannot  
 362 be directly measured but associated fields which are the observables. Electric (“**E**”)  
 363 and magnetic (“**B**”) fields in CED are associated with the electric scalar potential  
 364 “**V**” and the vector potential “**A**”. In particular, **E** can be obtained by measuring  
 365 the change in the space of the scalar potential ( $\Delta V$ ); however, two scalar potentials  
 366 differing by a constant “f” correspond to the same electric field. The same happens in  
 367 the case of the vector potential “**A**”; thus, different configurations of the associated  
 368 fields result in the same set of values of the observables. The freedom in choosing  
 369 one particular configuration is known as “gauge freedom”; the transformation law con-  
 370 necting two configurations is known as “gauge transformation” and the fact that the

371 observables are not affected by a gauge transformation is called “gauge invariance”.

372

373 When the gauge transformation:

$$\begin{aligned}\mathbf{A} &\rightarrow \mathbf{A} - \nabla f \\ V &\rightarrow V - \frac{\partial f}{\partial t}\end{aligned}\tag{2.4}$$

374 is applied to Maxwell equations, they are still satisfied and the fields remain invariant.

375 Thus, CED is invariant under gauge transformations and is called a “gauge theory”.

376 The set of all gauge transformations form the “symmetry group” of the theory, which

377 according to the group theory, has a set of “group generators”. The number of group

378 generators determine the number of “gauge fields” of the theory.

379

380 As mentioned in the first lines of section 2.2, QED has one symmetry group ( $U(1)$ )

381 with one group generator (the  $Q$  operator) and one gauge field (the electromagnetic

382 field  $A^\mu$ ). In CED there is not a clear definition, beyond the historical convention, of

383 which fields are the fundamental and which are the associated, but in QED it is clear

384 that the fundamental field is  $A^\mu$ . When a gauge theory is quantized, the gauge field

385 is quantized and its quanta is called “gauge boson”. The word boson characterizes

386 particles with integer spin which obvey Bose-einstein statistics.

387

388 As will be detailed in section 2.3, interactions between particles in a system can be

389 obtained by considering first the Lagrangian density of free particles in the system,

390 which of course is incomplete because the interaction terms have been left out, and

391 demanding global phase transformation invariance. Global phase transformation in-

392 variance means that a gauge transformation is performed identically to every point  
 393 in the space<sup>7</sup> and the Lagrangian remains invariant. Then, the global transformation  
 394 is promoted to a local phase transformation (this time the gauge transformation de-  
 395 pends on the position in space) and again invariance is required.

396

397 Due to the space dependence of the local tranformation, the Lagrangian density is  
 398 not invariant anymore. In order to restate the gauge invariance, the gauge covariant  
 399 derivative is introduced in the Lagrangian and with it the gauge field responsible for  
 400 the interaction between particles in the system. The new Lagrangian density is gauge  
 401 invariant, includes the interaction terms needed to account for the interactions and  
 402 provides a way to explain the interaction between particles through the exchange of  
 403 the gauge boson.

404 This recipe was used to build QED and the theories that aim to explain the funda-  
 405 mental interactions.

### 406 **2.2.3 Gauge bosons**

407 The importance of the gauge bosons comes from the fact that they are the force  
 408 mediators or force carriers. The features of the gauge bosons reflect those of the  
 409 fields they represent and they are extracted from the Lagrangian density used to  
 410 describe the interactions. In section 2.3, it will be shown how the gauge bosons of the  
 411 EI and WI emerge from the electroweak Lagrangian. The SI gauge bosons features  
 412 are also extracted from the SI Lagrangian but it is not detailed in this document. The  
 413 main features of the SM gauge bosons will be briefly presented below and summarized  
 414 in table 2.7.

---

<sup>7</sup> Here space corresponds to the 4-dimensional space i.e. space-time.

- 415     • **Photon.** EI occurs when the photon couples to (is exchanged between) particles  
 416       carrying electric charge; however, the photon itself does not carry electric charge,  
 417       therefore, there is no coupling between photons. Given that the photon is  
 418       massless the EI is of infinite range, i.e., electrically charged particles interact  
 419       even if they are located far away one from each other; this also implies that  
 420       photons always move with the speed of light.
- 421     • **Gluon.** SI is mediated by gluons which, same as photons, are massless. They  
 422       carry one unit of color charge and one unit of anticolor charge which means that  
 423       gluons couple to other gluons. As a result, the range of the SI is not infinite  
 424       but very short due to the attraction between gluons, giving rise to the “color  
 425       confinement” which explains why color charged particles cannot be isolated but  
 426       live within composited particles, like quarks inside protons.
- 427     • **W, Z.** The WI mediators,  $W^\pm$  and Z, are massive which explains their short-  
 428       range. Given that the WI is the only interaction that can change the flavor  
 429       of the interacting particles, the W boson is the responsible for the nuclear  
 430       transmutation where a neutron is converted in a proton or vice versa with the  
 431       involvement of an electron and a neutrino (see figure 2.4c). The Z boson is the  
 432       responsible of the neutral weak processes like neutrino elastic scattering where  
 433       no electric charge but momentum transference is involved. WI gauge bosons  
 434       carry isospin charge which makes possible the interaction between them.

Interaction	Mediator	Electric charge (e)	Color charge	Weak Isospin	mass (GeV/c <sup>2</sup> )
Electromagnetic	Photon ( $\gamma$ )	0	No	0	0
Strong	Gluon (g)	0	Yes -octet	No	0
Weak	$W^\pm$	$\pm 1$	No	$\pm 1$	$80.385 \pm 0.015$
	Z	0	No	0	$91.188 \pm 0.002$

**Table 2.7:** SM gauge bosons main features [9].

## 436 2.3 Electroweak unification and the Higgs

### 437 mechanism

438 Physicists dream of building a theory that contains all the interactions in one single  
 439 interaction, i.e., showing that at some scale in energy all the four fundamental in-  
 440 teractions are unified and only one interaction emerges in a “Theory of everything”.  
 441 The first sign of the feasibility of such unification comes from success in the con-  
 442 struction of the CED. Einstein spent years trying to reach that dream, which by  
 443 1920 only involved electromagnetism and gravity, with no success; however, a new  
 444 partial unification was achieved in the 1960’s, when S.Glashow [22], A.Salam [23] and  
 445 S.Weinberg [24] independently proposed that electromagnetic and weak interactions  
 446 are two manifestations of a more general interaction called “electroweak interaction  
 447 (EWT)”. Both, QCD and EWT, were developed in parallel and following the useful  
 448 prescription provided by QED and the gauge invariance principles.

449

450 The theory of weak interactions was capable of explaining the  $\beta$ -decay and in general  
 451 the processes mediated by  $W^\pm$  bosons. However, there were some processes like the  
 452 “ $\nu_\mu - e$  scattering” which would require the exchange of two W bosons (see figure 2.5  
 453 top diagrams) giving rise to divergent loop integrals and then non finite predictions.  
 454 By including neutral currents involving fermions via the exchange of neutral bosons  
 455 Z, those divergences are compensated and the predictions become realistic.

456

457 Neutral weak interaction vertices conserve flavor in the same way as the electromag-  
 458 netic vertices do, but additionally, the Z boson can couple to neutrinos which implies  
 459 that processes involving charged fermions can proceed through EI or WI but processes  
 460 involving neutrinos can proceed only through WI.

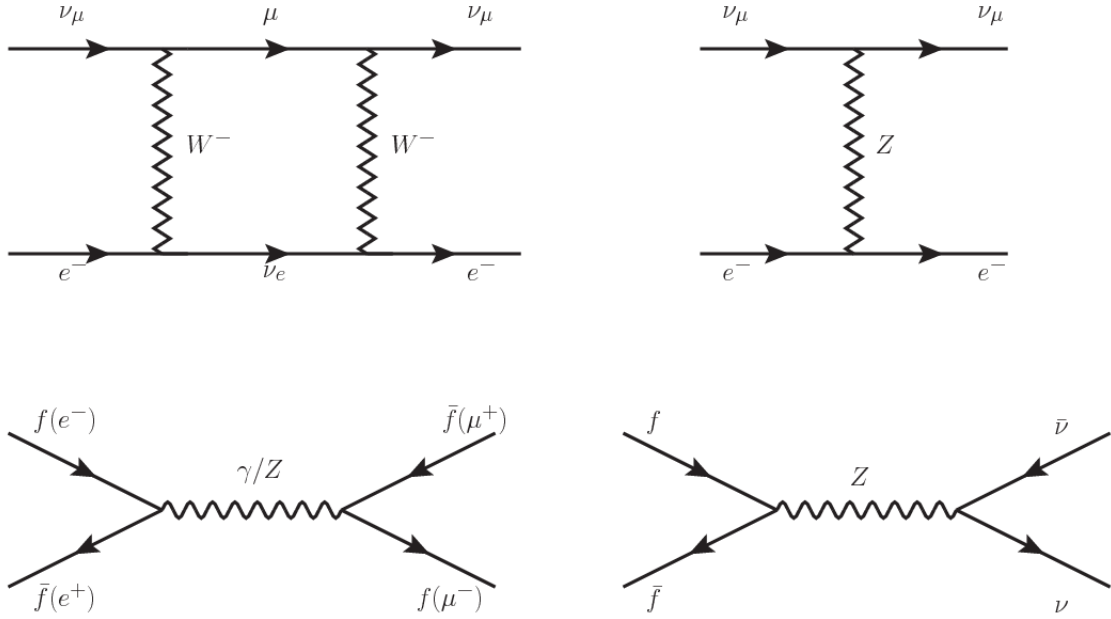


**Figure 2.5:** Top:  $\nu_\mu - e^-$  scattering going through charged currents (left) and neutral currents (right). Bottom: neutral current processes for charged fermions (left) and involving neutrinos (right). While neutral current processes involving only charged fermions can proceed through EI or WI, those involving neutrinos can only proceed via WI.

461

462 The prescription to build a gauge theory of the WI consists of proposing a free field  
 463 Lagrangian density that includes the particles involved; next, by requesting invari-  
 464 ance under global phase transformations first and generalizing to local phase trans-  
 465 formations invariance later, the conserved currents are identified and interactions are  
 466 generated by introducing gauge fields. Given that the goal is to include the EI and  
 467 WI in a single theory, the group symmetry considered should be a combination of  
 468  $SU(2)_L$  and  $U(1)_{em}$ , however the latter cannot be used directly because the EI treats  
 469 left and right-handed particles indistinctly in contrast to the former. Fortunately, the  
 470 weak hypercharge, which is a combination of the weak isospin and the electric charge  
 471 (eqn 2.2) is suitable to be used since it is conserved by the EI and WI. Thus, the  
 472 symmetry group to be considered is

$$G \equiv SU(2)_L \otimes U(1)_Y \quad (2.5)$$

473 The following treatment applies to any of the fermion generations, but for simplicity  
 474 the first generation of leptons will be considered [5, 6, 25, 26].

475

476 Given the first generation of leptons

$$\psi_1 = \begin{pmatrix} \nu_e \\ e^- \end{pmatrix}_L, \quad \psi_2 = \nu_{eR}, \quad \psi_3 = e_R^- \quad (2.6)$$

477 the charged fermionic currents are given by

$$J_\mu \equiv J_\mu^+ = \bar{\nu}_{eL} \gamma_\mu e_L, \quad J_\mu^\dagger \equiv J_\mu^- = \bar{e}_L \gamma_\mu \nu_{eL} \quad (2.7)$$

478 and the free Lagrangian is given by

$$\mathcal{L}_0 = \sum_{j=1}^3 i\bar{\psi}_j(x) \gamma^\mu \partial_\mu \psi_j(x). \quad (2.8)$$

479 Mass terms are included directly in the QED and QCD free Lagrangians since they  
 480 preserve the invariance under the symmetry transformations involved which treat  
 481 left-handed and right-handed similarly, however mass terms of the form

$$m_W^2 W_\mu^\dagger(x) W^\mu(x) + \frac{1}{2} m_Z^2 Z_\mu(x) Z^\mu(x) - m_e \bar{\psi}_e(x) \psi_e(x) \quad (2.9)$$

482 which represent the mass of  $W^\pm$ , Z and electrons, are not invariant under G trans-  
 483 formations, therefore the gauge fields described by the EWI are in principle massless.

484

485 Experiments have shown that the gauge fields are not massless; however, they have

486 to acquire mass through a mechanism compatible with the gauge invariance; that  
 487 mechanism is known as the “Higgs mechanism” and will be considered later in this  
 488 section. The global transformations in the combined symmetry group  $G$  can be  
 489 written as

$$\begin{aligned}\psi_1(x) &\xrightarrow{G} \psi'_1(x) \equiv U_Y U_L \psi_1(x), \\ \psi_2(x) &\xrightarrow{G} \psi'_2(x) \equiv U_Y \psi_2(x), \\ \psi_3(x) &\xrightarrow{G} \psi'_3(x) \equiv U_Y \psi_3(x)\end{aligned}\tag{2.10}$$

490 where  $U_L$  represent the  $SU(2)_L$  transformation acting only on the weak isospin dou-  
 491 blet and  $U_Y$  represent the  $U(1)_Y$  transformation acting on all the weak isospin mul-  
 492 tiplets. Explicitly

$$U_L \equiv \exp\left(i\frac{\sigma_i}{2}\alpha^i\right), \quad U_Y \equiv \exp(iy_i\beta) \quad (i = 1, 2, 3)\tag{2.11}$$

493 with  $\sigma_i$  the Pauli matrices and  $y_i$  the weak hypercharges. In order to promote the  
 494 transformations from global to local while keeping the invariance, it is required that  
 495  $\alpha^i = \alpha^i(x)$ ,  $\beta = \beta(x)$  and the replacement of the ordinary derivatives by the covariant  
 496 derivatives

$$\begin{aligned}D_\mu \psi_1(x) &\equiv [\partial_\mu + ig\sigma_i W_\mu^i(x)/2 + ig'y_1 B_\mu(x)] \psi_1(x) \\ D_\mu \psi_2(x) &\equiv [\partial_\mu + ig'y_2 B_\mu(x)] \psi_2(x) \\ D_\mu \psi_3(x) &\equiv [\partial_\mu + ig'y_3 B_\mu(x)] \psi_3(x)\end{aligned}\tag{2.12}$$

497 introducing in this way four gauge fields,  $W_\mu^i(x)$  and  $B_\mu(x)$ , in the process. The  
 498 covariant derivatives (eqn 2.12) are required to transform in the same way as fermion  
 499 fields  $\psi_i(x)$  themselves, therefore, the gauge fields transform as:

$$\begin{aligned} B_\mu(x) &\xrightarrow{G} B'_\mu(x) \equiv B_\mu(x) - \frac{1}{g'} \partial_\mu \beta(x) \\ W_\mu^i(x) &\xrightarrow{G} W_\mu^{i\prime}(x) \equiv W_\mu^i(x) - \frac{i}{g} \partial_\mu \alpha_i(x) - \varepsilon_{ijk} \alpha_i(x) W_\mu^j(x). \end{aligned} \quad (2.13)$$

500 The G invariant version of the Lagrangian density 2.8 can be written as

$$\mathcal{L}_0 = \sum_{j=1}^3 i \bar{\psi}_j(x) \gamma^\mu D_\mu \psi_j(x) \quad (2.14)$$

501 where free massless fermion and gauge fields and fermion-gauge boson interactions  
 502 are included. The EWI Lagrangian density must additionally include kinetic terms  
 503 for the gauge fields ( $\mathcal{L}_G$ ) which are built from the field strengths, according to

$$B_{\mu\nu}(x) \equiv \partial_\mu B_\nu - \partial_\nu B_\mu \quad (2.15)$$

$$W_{\mu\nu}^i(x) \equiv \partial_\mu W_\nu^i(x) - \partial_\nu W_\mu^i(x) - g \varepsilon^{ijk} W_\mu^j W_\nu^k \quad (2.16)$$

504 the last term in eqn. 2.16 is added in order to hold the gauge invariance; therefore,

$$\mathcal{L}_G = -\frac{1}{4} B_{\mu\nu}(x) B^{\mu\nu}(x) - \frac{1}{4} W_{\mu\nu}^i(x) W_i^{\mu\nu}(x) \quad (2.17)$$

505 which contains not only the free gauge fields contributions, but also the gauge fields  
 506 self-interactions and interactions among them.

508 The three weak isospin conserved currents resulting from the  $SU(2)_L$  symmetry are  
 509 given by

$$J_\mu^i(x) = \frac{1}{2} \bar{\psi}_1(x) \gamma_\mu \sigma^i \psi_1(x) \quad (2.18)$$

510 while the weak hypercharge conserved current resulting from the  $U(1)_Y$  symmetry is  
 511 given by

$$J_\mu^Y = \sum_{j=1}^3 \bar{\psi}_j(x) \gamma_\mu y_j \psi_j(x) \quad (2.19)$$

512 In order to evaluate the electroweak interactions modeled by an isovector field  $W_\mu^i$   
 513 which couples to isospin currents  $J_\mu^i$  with strength  $g$  and additionally the singlet  
 514 field  $B_\mu$  which couples to the weak hypercharge current  $J_\mu^Y$  with strength  $g'/2$ . The  
 515 interaction Lagrangian density to be considered is

$$\mathcal{L}_I = -g J^{i\mu}(x) W_\mu^i(x) - \frac{g'}{2} J^{Y\mu}(x) B_\mu(x) \quad (2.20)$$

516 Note that the weak isospin currents are not the same as the charged fermionic currents  
 517 that were used to describe the WI (eqn 2.7), since the weak isospin eigenstates are  
 518 not the same as the mass eigenstates, but they are closely related

$$J_\mu = \frac{1}{2} (J_\mu^1 + i J_\mu^2), \quad J_\mu^\dagger = \frac{1}{2} (J_\mu^1 - i J_\mu^2). \quad (2.21)$$

519 The same happens with the gauge fields  $W_\mu^i$  which are related to the mass eigenstates  
 520  $W^\pm$  by

$$W_\mu^+ = \frac{1}{\sqrt{2}} (W_\mu^1 - i W_\mu^2), \quad W_\mu^- = \frac{1}{\sqrt{2}} (W_\mu^1 + i W_\mu^2). \quad (2.22)$$

521 The fact that there are three weak isospin conserved currents is an indication that in  
 522 addition to the charged fermionic currents, which couple charged to neutral leptons,  
 523 there should be a neutral fermionic current that does not involve electric charge  
 524 exchange; therefore, it couples neutral fermions or fermions of the same electric charge.  
 525 The third weak isospin current contains a term that is similar to the electromagnetic  
 526 current ( $j_\mu^{em}$ ), indicating that there is a relation between them and resembling the  
 527 Gell-Mann-Nishijima formula 2.2 adapted to electroweak interactions

$$Q = T_3 + \frac{Y_W}{2}. \quad (2.23)$$

528 Just as Q generates the  $U(1)_{em}$  symmetry, the weak hypercharge generates the  $U(1)_Y$   
 529 symmetry as said before. It is possible to write the relationship in terms of the currents  
 530 as

$$j_\mu^{em} = J_\mu^3 + \frac{1}{2}J_\mu^Y. \quad (2.24)$$

531 The neutral gauge fields  $W_\mu^3$  and  $B_\mu$  cannot be directly identified with the  $Z$  and the  
 532 photon fields since the photon interacts similarly with left and right-handed fermions;  
 533 however, they are related through a linear combination given by

$$\begin{aligned} A_\mu &= B_\mu \cos \theta_W + W_\mu^3 \sin \theta_W \\ Z_\mu &= -B_\mu \sin \theta_W + W_\mu^3 \cos \theta_W \end{aligned} \quad (2.25)$$

534 where  $\theta_W$  is known as the “Weinberg angle.” The interaction Lagrangian is now given

535 by

$$\mathcal{L}_I = -\frac{g}{\sqrt{2}}(J^\mu W_\mu^+ + J^{\mu\dagger} W_\mu^-) - \left(g \sin \theta_W J_\mu^3 + g' \cos \theta_W \frac{J_\mu^Y}{2}\right) A^\mu - \left(g \cos \theta_W J_\mu^3 - g' \sin \theta_W \frac{J_\mu^Y}{2}\right) Z^\mu \quad (2.26)$$

536 the first term is the weak charged current interaction, while the second term is the  
537 electromagnetic interaction under the condition

$$g \sin \theta_W = g' \cos \theta_W = e, \quad \frac{g'}{g} = \tan \theta_W \quad (2.27)$$

538 contained in the eqn.2.24; the third term is the neutral weak current.

539

540 Note that the neutral fields transformation given by the eqn. 2.25 can be written in  
541 terms of the coupling constants  $g$  and  $g'$  as:

$$A_\mu = \frac{g' W_\mu^3 + g B_\mu}{\sqrt{g^2 + g'^2}}, \quad Z_\mu = \frac{g W_\mu^3 - g' B_\mu}{\sqrt{g^2 + g'^2}} \quad (2.28)$$

542 So far, the Lagrangian density describing the non-massive EWI is:

$$\mathcal{L}_{nmEWI} = \mathcal{L}_0 + \mathcal{L}_G \quad (2.29)$$

543 where fermion and gauge fields have been considered massless because their regular  
544 mass terms are manifestly non invariant under G transformations; therefore, masses  
545 have to be generated in a gauge invariant way. The mechanism by which this goal is  
546 achieved is known as the “Higgs mechanism” and is closely connected to the concept  
547 of “spontaneous symmetry breaking.”

548 **2.3.1 Spontaneous symmetry breaking (SSB)**

549 Figure 2.6 left shows a steel nail (top) which is subject to an external force; the form  
 550 of the potential energy is also shown (bottom).

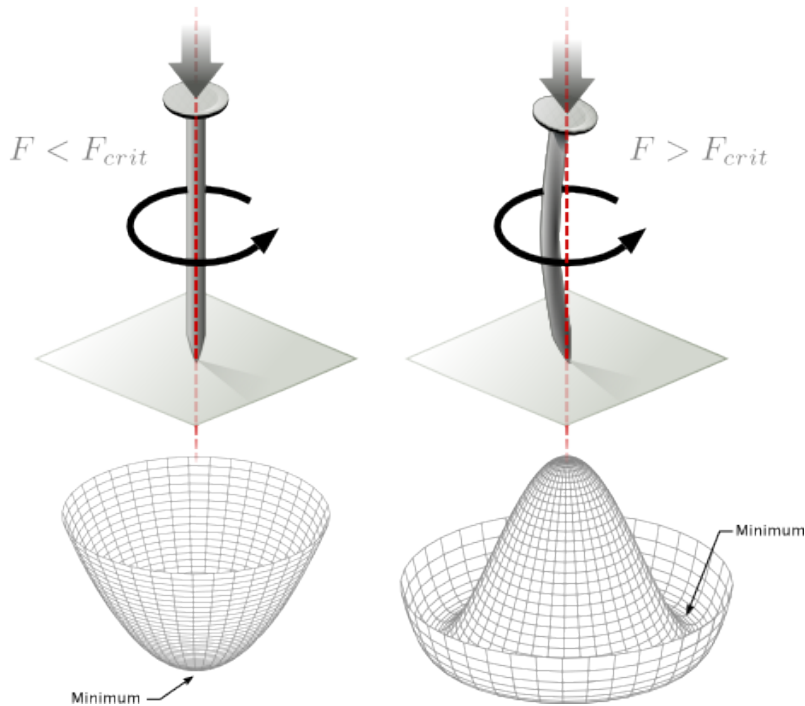


**Figure 2.6:** Spontaneous symmetry breaking mechanism. The steel nail, subject to an external force (top left), has rotational symmetry with respect to its axis. When the external force overcomes a critical value the nail buckles (top right) choosing a minimal energy state (ground state) and thus “*breaking spontaneously the rotational symmetry*”. The potential energy (bottom) changes but holds the rotational symmetry; however, an infinite number of asymmetric ground states are generated and circularly distributed in the bottom of the potential [27].

551

552 Before reaching the critical force value, the system has rotational symmetry with re-  
 553 spect to the nail axis; however, after the critical force value is reached the nail buckles  
 554 (top right). The form of the potential energy (bottom right) changes, preserving its  
 555 rotational symmetry although its minima does not exhibit that rotational symmetry  
 556 any longer. Right before the nail buckles there is no indication of the direction the

557 nail will bend because any of the directions are equivalent, but once the nail bends,  
 558 choosing a direction, an arbitrary minimal energy state (ground state) is selected and  
 559 it does not share the system's rotational symmetry. This mechanism for reaching an  
 560 asymmetric ground state is known as "*spontaneous symmetry breaking*".

561 The lesson from this analysis is that the way to introduce the SSB mechanism into a  
 562 system is by adding the appropriate potential to it.

563

564 Figure 2.7 shows a plot of the potential  $V(\phi)$  in the case of a scalar field  $\phi$

$$V(\phi) = \mu^2 \phi^\dagger \phi + \lambda (\phi^\dagger \phi)^2 \quad (2.30)$$

565 If  $\mu^2 > 0$  the potential has only one minimum at  $\phi = 0$  and describes a scalar field  
 566 with mass  $\mu$ . If  $\mu^2 < 0$  the potential has a local maximum at  $\phi = 0$  and two minima  
 567 at  $\phi = \pm\sqrt{-\mu^2/\lambda}$  which enables the SSB mechanism to work.

568

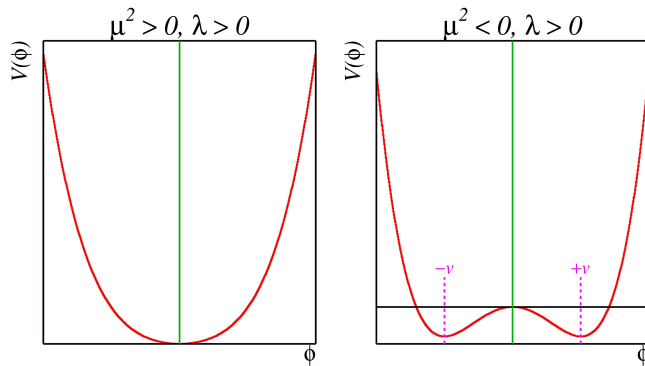


**Figure 2.7:** Shape of the potential  $V(\phi)$  for  $\lambda > 0$  and:  $\mu^2 > 0$  (left) and  $\mu^2 < 0$  (right). The case  $\mu^2 < 0$  corresponds to the potential suitable for introducing the SSB mechanism by choosing one of the two ground states which are connected via reflection symmetry. [27].

569 In the case of a complex scalar field  $\phi(x)$

$$\phi(x) = \frac{1}{\sqrt{2}}(\phi_1 + i\phi_2) \quad (2.31)$$

570 the Lagrangian (invariant under global  $U(1)$  transformations) is given by

$$\mathcal{L} = (\partial_\mu \phi)^\dagger (\partial^\mu \phi) - V(\phi), \quad V(\phi) = \mu^2 \phi^\dagger \phi + \lambda (\phi^\dagger \phi)^2 \quad (2.32)$$

571 where an appropriate potential has been added in order to introduce the SSB.

572

573 As seen in figure 2.8, the potential has now an infinite number of minima circularly  
 574 distributed along the  $\xi$ -direction which makes possible the occurrence of the SSB by  
 575 choosing an arbitrary ground state; for instance,  $\xi = 0$ , i.e.  $\phi_1 = v, \phi_2 = 0$

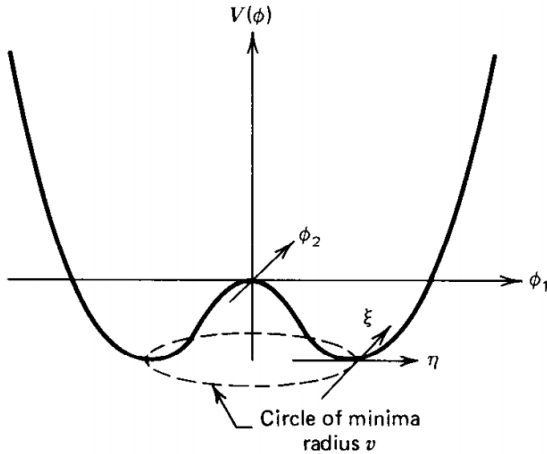


**Figure 2.8:** Potential for complex scalar field. There is a circle of minima of radius  $v$  along the  $\xi$ -direction [6].

$$\phi_0 = \frac{v}{\sqrt{2}} \exp(i\xi) \xrightarrow{SSB} \phi_0 = \frac{v}{\sqrt{2}} \quad (2.33)$$

576 As usual, excitations over the ground state are studied by making an expansion about

577 it; thus, the excitation can be parametrized as:

$$\phi(x) = \frac{1}{\sqrt{2}}(v + \eta(x) + i\xi(x)) \quad (2.34)$$

578 which when substituted into eqn. 2.32 produces a Lagrangian in terms of the new  
 579 fields  $\eta$  and  $\xi$

$$\mathcal{L}' = \frac{1}{2}(\partial_\mu\xi)^2 + \frac{1}{2}(\partial_\mu\eta)^2 + \mu^2\eta^2 - V(\phi_0) - \lambda v\eta(\eta^2 + \xi^2) - \frac{\lambda}{4}(\eta^2 + \xi^2)^2 \quad (2.35)$$

580 where the last two terms represent the interactions and self-interaction between the  
 581 two fields  $\eta$  and  $\xi$ . The particular feature of the SSB mechanism is revealed when  
 582 looking to the first three terms of  $\mathcal{L}'$ . Before the SSB, only the massless  $\phi$  field is  
 583 present in the system; after the SSB there are two fields of which the  $\eta$ -field has  
 584 acquired mass  $m_\eta = \sqrt{-2\mu^2}$  while the  $\xi$ -field is still massless (see figure 2.9).

585

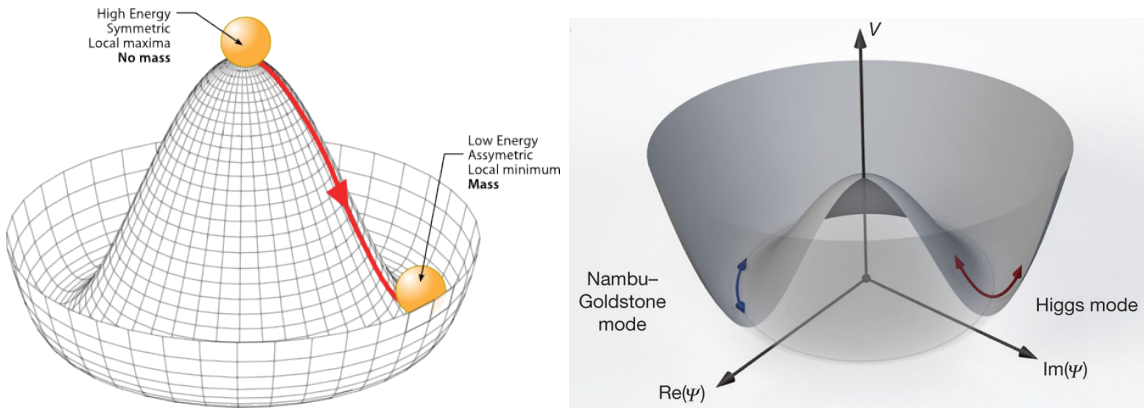


**Figure 2.9:** SSB mechanism for a complex scalar field [27, 28].

586 Thus, the SSB mechanism serves as a method to generate mass but as a side effect a  
 587 massless field is introduced in the system. This fact is known as the Goldstone theorem

and states that a massless scalar field appears in the system for each continuous symmetry spontaneously broken. Another version of the Goldstone theorem states that “*if a Lagrangian is invariant under a continuous symmetry group  $G$ , but the vacuum is only invariant under a subgroup  $H \subset G$ , then there must exist as many massless spin-0 particles (Nambu-Goldstone bosons) as broken generators.*” [26] The Nambu-Goldstone boson can be understood considering that the potential in the  $\xi$ -direction is flat so excitations in that direction are not energy consuming and thus represent a massless state.

### 2.3.2 Higgs mechanism

When the SSB mechanism is introduced in the formulation of the EWI in an attempt to generate the mass of the so far massless gauge bosons and fermions, an interesting effect is revealed. In order to keep the  $G$  symmetry group invariance and generate the mass of the EW gauge bosons, a  $G$  invariant Lagrangian density ( $\mathcal{L}_S$ ) has to be added to the non massive EWI Lagrangian (eqn. 2.29)

$$\mathcal{L}_S = (D_\mu \phi)^\dagger (D^\mu \phi) - \mu^2 \phi^\dagger \phi - \lambda (\phi^\dagger \phi)^2, \quad \lambda > 0, \mu^2 < 0 \quad (2.36)$$

$$D_\mu \phi = \left( i\partial_\mu - g \frac{\sigma_i}{2} W_\mu^i - g' \frac{Y}{2} B_\mu \right) \phi \quad (2.37)$$

$\phi$  has to be an isospin doublet of complex scalar fields so it preserves the  $G$  invariance; thus  $\phi$  can be defined as:

$$\phi = \begin{pmatrix} \phi^+ \\ \phi^0 \end{pmatrix} \equiv \frac{1}{\sqrt{2}} \begin{pmatrix} \phi_1 + i\phi_2 \\ \phi_3 + i\phi_4 \end{pmatrix}. \quad (2.38)$$

The minima of the potential are defined by

$$\phi^\dagger \phi = \frac{1}{2}(\phi_1^2 + \phi_2^2 + \phi_3^2 + \phi_4^2) = -\frac{\mu^2}{2\lambda}. \quad (2.39)$$

605 The choice of the ground state is critical. By choosing a ground state, invariant under  
 606  $U(1)_{em}$  gauge symmetry, the photon will remain massless and the  $W^\pm$  and  $Z$  bosons  
 607 masses will be generated which is exactly what is needed. In that sense, the best  
 608 choice corresponds to a weak isospin doublet with  $T_3 = -1/2$ ,  $Y_W = 1$  and  $Q = 0$   
 609 which defines a ground state with  $\phi_1 = \phi_2 = \phi_4$  and  $\phi_3 = v$ :

$$\phi_0 \equiv \frac{1}{\sqrt{2}} \begin{pmatrix} 0 \\ v \end{pmatrix}, \quad v^2 \equiv -\frac{\mu^2}{\lambda}. \quad (2.40)$$

610 where the vacuum expectation value  $v$  is fixed by the Fermi coupling  $G_F$  according  
 611 to  $v = (\sqrt{2}G_F)^{1/2} \approx 246$  GeV.

612

613 The G symmetry has been broken and three Nambu-Goldstone bosons will appear.  
 614 The next step is to expand  $\phi$  about the chosen ground state as:

$$\phi(x) = \frac{1}{\sqrt{2}} \exp\left(\frac{i}{v} \sigma_i \theta^i(x)\right) \begin{pmatrix} 0 \\ v + H(x) \end{pmatrix} \approx \frac{1}{\sqrt{2}} \begin{pmatrix} \theta_1(x) + i\theta_2(x) \\ v + H(x) - i\theta_3(x) \end{pmatrix} \quad (2.41)$$

615 to describe fluctuations from the ground state  $\phi_0$ . The fields  $\theta_i(x)$  represent the  
 616 Nambu-Goldstone bosons while  $H(x)$  is known as “higgs field.” The fundamental  
 617 feature of the parametrization used is that the dependence on the  $\theta_i(x)$  fields is  
 618 factored out in a global phase that can be eliminated by taking the physical “unitary  
 619 gauge”  $\theta_i(x) = 0$ . Therefore the expansion about the ground state is given by:

$$\phi(x) \frac{1}{\sqrt{2}} \begin{pmatrix} 0 \\ v + H(x) \end{pmatrix} \quad (2.42)$$

620 which when substituted into  $\mathcal{L}_S$  (eqn. 2.36) results in a Lagrangian containing the now  
 621 massive three gauge bosons  $W^\pm, Z$ , one massless gauge boson (photon) and the new  
 622 Higgs field ( $H$ ). The three degrees of freedom corresponding to the Nambu-Goldstone  
 623 bosons are now integrated into the massive gauge bosons as their longitudinal po-  
 624 larizations which were not available when they were massless particles. The effect  
 625 by which vector boson fields acquire mass after an spontaneous symmetry breaking,  
 626 but without an explicit gauge invariance breaking is known as the “*Higgs mechanism*”.

627

628 The mechanism was proposed by three independent groups: F.Englert and R.Brout  
 629 in August 1964 [29], P.Higgs in October 1964 [30] and G.Guralnik, C.Hagen and  
 630 T.Kibble in November 1964 [31]; however, its importance was not realized until  
 631 S.Glashow [22], A.Salam [23] and S.Weinberg [24], independently, proposed that elec-  
 632 tromagnetic and weak interactions are two manifestations of a more general interac-  
 633 tion called “electroweak interaction” in 1967.

### 634 2.3.3 Masses of the gauge bosons

635 The mass of the gauge bosons is extracted by evaluating the kinetic part of Lagrangian  
 636  $\mathcal{L}_S$  in the ground state (known also as the vacuum expectation value), i.e.,

$$\left| \left( \partial_\mu - ig \frac{\sigma_i}{2} W_\mu^i - i \frac{g'}{2} B_\mu \right) \phi_0 \right|^2 = \left( \frac{1}{2} v g \right)^2 W_\mu^+ W^{-\mu} + \frac{1}{8} v^2 (W_\mu^3, B_\mu) \begin{pmatrix} g^2 & -gg' \\ -gg' & g'^2 \end{pmatrix} \begin{pmatrix} W^{3\mu} \\ B^\mu \end{pmatrix} \quad (2.43)$$

637 comparing with the typical mass term for a charged boson  $M_W^2 W^+ W^-$

$$M_W = \frac{1}{2} v g. \quad (2.44)$$

The second term in the right side of the eqn.2.43 comprises the masses of the neutral

bosons, but it needs to be written in terms of the gauge fields  $Z_\mu$  and  $A_\mu$  in order to be compared to the typical mass terms for neutral bosons, therefore using eqn. 2.28

$$\begin{aligned} \frac{1}{8}v^2[g^2(W_\mu^3)^2 - 2gg'W_\mu^3B^\mu + g'^2B_\mu^2] &= \frac{1}{8}v^2[gW_\mu^3 - g'B_\mu]^2 + 0[g'W_\mu^3 + gB_\mu]^2 \\ &= \frac{1}{8}v^2[\sqrt{g^2 + g'^2}Z_\mu]^2 + 0[\sqrt{g^2 + g'^2}A_\mu]^2 \end{aligned} \quad (2.45)$$

638 and then

$$M_Z = \frac{1}{2}v\sqrt{g^2 + g'^2}, \quad M_A = 0 \quad (2.46)$$

### 639 2.3.4 Masses of the fermions

640 The lepton mass terms can be generated by introducing a gauge invariant Lagrangian  
641 term describing the Yukawa coupling between the lepton field and the Higgs field

$$\mathcal{L}_{Yl} = -G_l \left[ (\bar{\nu}_l, \bar{l})_L \begin{pmatrix} \phi^+ \\ \phi^0 \end{pmatrix} l_R + \bar{l}_R (\phi^-, \bar{\phi}^0) \begin{pmatrix} \nu_l \\ l \end{pmatrix}_L \right], \quad l = e, \mu, \tau. \quad (2.47)$$

642 After the SSB and replacing the usual field expansion about the ground state (eqn.2.40)  
643 into  $\mathcal{L}_{Yl}$ , the mass term arises

$$\mathcal{L}_{Yl} = -m_l(\bar{l}_L l_R + \bar{l}_R l_L) - \frac{m_l}{v}(\bar{l}_L l_R + \bar{l}_R l_L)H = -m_l \bar{l} \left( 1 + \frac{H}{v} \right) \quad (2.48)$$

644

$$m_l = \frac{G_l}{\sqrt{2}}v \quad (2.49)$$

645 where the additional term represents the lepton-Higgs interaction. The quark masses  
646 are generated in a similar way as lepton masses but for the upper member of the

647 quark doublet a different Higgs doublet is needed:

$$\phi_c = -i\sigma_2\phi^* = \begin{pmatrix} -\bar{\phi}^0 \\ \phi^- \end{pmatrix}. \quad (2.50)$$

648 Additionally, given that the quark isospin doublets are not constructed in terms of  
 649 the mass eigenstates but in terms of the flavor eigenstates, as shown in table 2.5, the  
 650 coupling parameters will be related to the CKM matrix elements; thus the quark  
 651 Lagrangian is given by:

$$\mathcal{L}_{Yq} = -G_d^{i,j}(\bar{u}_i, \bar{d}_i)_L \begin{pmatrix} \phi^+ \\ \phi^0 \end{pmatrix} d_{jR} - G_u^{i,j}(\bar{u}_i, \bar{d}_i)_L \begin{pmatrix} -\bar{\phi}^0 \\ \phi^- \end{pmatrix} u_{jR} + h.c. \quad (2.51)$$

652 with  $i,j=1,2,3$ . After SSB and expansion about the ground state, the diagonal form  
 653 of  $\mathcal{L}_{Yq}$  is:

$$\mathcal{L}_{Yq} = -m_d^i \bar{d}_i d_i \left( 1 + \frac{H}{v} \right) - m_u^i \bar{u}_i u_i \left( 1 + \frac{H}{v} \right) \quad (2.52)$$

654 Fermion masses depend on arbitrary couplings  $G_l$  and  $G_{u,d}$  and are not predicted by  
 655 the theory.

### 656 2.3.5 The Higgs field

657 After the characterization of the fermions and gauge bosons as well as their interac-  
 658 tions, it is necessary to characterize the Higgs field itself. The Lagrangian  $\mathcal{L}_S$  in eqn.  
 659 2.3.6 written in terms of the gauge bosons is given by

$$\mathcal{L}_S = \frac{1}{4}\lambda v^4 + \mathcal{L}_H + \mathcal{L}_{HV} \quad (2.53)$$

660

$$\mathcal{L}_H = \frac{1}{2}\partial_\mu H \partial^\mu H - \frac{1}{2}m_H^2 H^2 - \frac{1}{2v}m_H^2 H^3 - \frac{1}{8v^2}m_H^2 H^4 \quad (2.54)$$

661

$$\mathcal{L}_{HV} = m_H^2 W_\mu^+ W^{\mu-} \left( 1 + \frac{2}{v}H + \frac{2}{v^2}H^2 \right) + \frac{1}{2}m_Z^2 Z_\mu Z^\mu \left( 1 + \frac{2}{v}H + \frac{2}{v^2}H^2 \right) \quad (2.55)$$

662 The mass of the Higgs boson is deduced as usual from the mass term in the Lagrangian  
 663 resulting in:

$$m_H = \sqrt{-2\mu^2} = \sqrt{2\lambda}v \quad (2.56)$$

664 however, it is not predicted by the theory either. The experimental efforts to find  
 665 the Higgs boson, carried out by the “Compact Muon Solenoid (CMS)” experiment  
 666 and the “A Toroidal LHC AppartuS (ATLAS)” experiments at the “Large Hadron  
 667 Collider(LHC)”, gave great results by July of 2012 when the discovery of a new  
 668 particle compatible with the Higgs boson predicted by the electroweak theory [32, 33]  
 669 was announced. Although at the announcement time there were some reservations  
 670 about calling the new particle the “Higgs boson”, today this name is widely accepted.  
 671 The Higgs mass measurement, reported by both experiments [34], is in table 2.8.

Property	Value
Electric charge	0
Colour charge	0
Spin	0
Weak isospin	-1/2
Weak hypercharge	1
Parity	1
Mass (GeV/c <sup>2</sup> )	125.09±0.21 (stat.)±0.11 (syst.)

**Table 2.8:** Higgs boson properties. Higgs mass is not predicted by the theory and the value here corresponds to the experimental measurement.

672

### 673 2.3.6 Production of Higgs bosons at LHC

674 At LHC, Higgs boson is produced as a result of the collision of two counter-rotating  
 675 protons beams. A detailed description of the LHC machine will be presented in  
 676 chapter 3. “The total cross section” is a parameter that quantifies the number of pp  
 677 collisions that happen when a number of protons are fired at each other. Different  
 678 results can be obtained after a pp collision and for each one the “cross section” is

679 defined as the number of pp collisions that conclude in that particular result with  
 respect to the number of protons fired at each other.

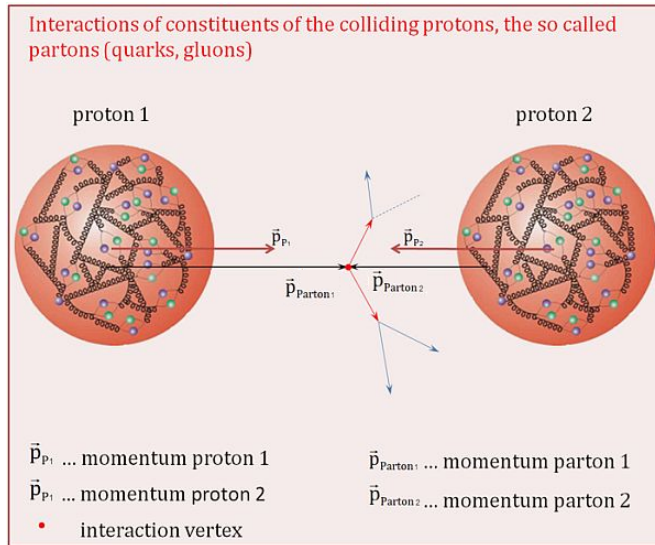


**Figure 2.10:** Proton-proton collision. Protons are composed of 3 valence quarks, a sea of quarks and gluons; therefore in a proton-proton collision, quarks and gluons are those who collide. [35].

680

681 Protons are composed of quarks and these quarks are bound by gluons; however,  
682 what is commonly called the quark content of the proton makes reference to the  
683 valence quarks. A sea of quarks and gluons is also present inside the proton as repre-  
684 sented in figure 2.10. In a proton-proton (pp) collision, the constituents (quarks and  
685 gluons) are those who collide. The pp cross section depends on the momentum of  
686 the colliding particles, reason for which it is needed to know how the momentum is  
687 distributed inside the proton. Quarks and gluons are known as partons and the func-  
688 tions that describe how the proton momentum is distributed among partons inside it  
689 are called “parton distribution functions (PDFs)”; PDFs are determined from experi-  
690 mental data obtained in experiments where the internal structure of hadrons is tested.

691

<sup>692</sup> In addition, in physics, a common approach to study complex systems consists in

693 starting with a simpler version of them, for which a well known description is avail-  
 694 able, and add an additional “perturbation” which represents a small deviation from  
 695 the known behavior. If the perturbation is small enough, the physical quantities as-  
 696 sociated with the perturbed system are expressed as a series of corrections to those  
 697 of the simpler system; therefore, the more terms are considered in the series (the  
 698 higher order in the perturbation series), the more precise is the the description of the  
 699 complex system.

700

701 This thesis explores the Higgs production at LHC; therefore the overview presented  
 702 here will be oriented specifically to the production mechanisms after pp collisions at  
 703 LHC.

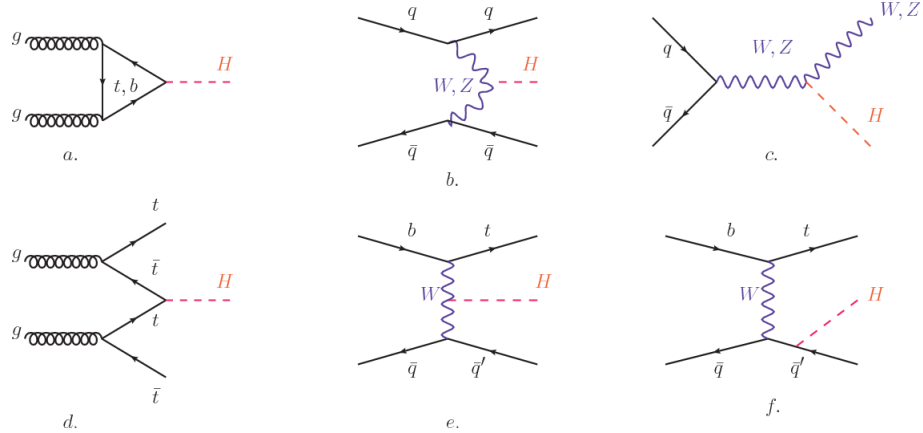


**Figure 2.11:** Main Higgs boson production mechanism Feynman diagrams. a. gluon-gluon fusion, b. vector boson fusion (VBF), c. Higgs-strahlung, d. Associated production with a top or bottom quark pair, e-f. associated production with a single top quark.

704 Figure 2.11 shows the Feynman diagrams for the leading order (first order) Higgs  
 705 production processes at LHC, while the cross section for Higgs production as a func-  
 706 tion of the center of mass-energy ( $\sqrt{s}$ ) for pp collisions is showed in figure 2.12 left.  
 707 The tags NLO (next to leading order), NNLO (next to next to leading order) and  
 708 N3LO (next to next to next to leading order) make reference to the order at which

the perturbation series have been considered.

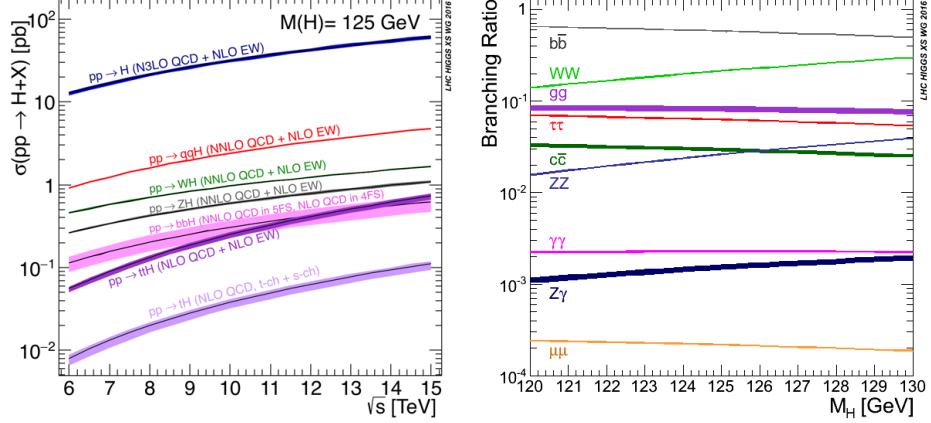


**Figure 2.12:** Higgs boson production cross sections (left) and decay branching ratios (right) for the main mechanisms. The VBF is indicated as  $q\bar{q}H$  [36].

As shown in eqns 2.47, 2.51 and 2.55, the strength of the Higgs-fermion interaction is proportional to the fermion mass while the strength of the Higgs-gauge boson interaction is proportional to the square of the gauge boson mass, which implies that the Higgs production and decay mechanisms are dominated by couplings  $H - (W, Z, t, b, \tau)$ .

The main production mechanism is the gluon fusion (figure 2.11a and  $pp \rightarrow H$  in figure 2.12) given that gluons carry the highest fraction of momentum of the protons in pp colliders. Since the Higgs boson does not couple to gluons, the mechanism proceeds through the exchange of a virtual top-quark loop given that for it the coupling is the biggest. Note that in this process, the Higgs boson is produced alone, which makes this mechanism experimentally clean when combined with the two-photon or the four-lepton decay channels (see section 2.3.7).

Vector boson fusion (figure 2.11b and  $pp \rightarrow q\bar{q}H$  in figure 2.12) has the second largest production cross section. The scattering of two fermions is mediated by a weak gauge boson which later emits a Higgs boson. In the final state, the two fermions

725 tend to be located in a particular region of the detector which is used as a signature  
 726 when analyzing the datasets provided by the experiments. More details about how  
 727 to identify events of interest in an analysis will be given in chapter ??.

728 The next production mechanism is Higgs-strahlung (figure 2.11c and  $pp \rightarrow WH, pp \rightarrow$   
 729  $ZH$  in figure 2.12) where two fermions annihilate to form a weak gauge boson. If the  
 730 initial fermions have enough energy, the emergent boson eventually will emit a Higgs  
 731 boson.

732 The associated production with a top or bottom quark pair and the associated pro-  
 733 duction with a single top quark (figure 2.11d-f and  $pp \rightarrow bbH, pp \rightarrow t\bar{t}H, pp \rightarrow tH$   
 734 in figure 2.12) have a smaller cross section than the main three mechanisms above,  
 735 but they provide a good opportunity to test the Higgs-top coupling. The analysis  
 736 reported in this thesis is developed using these production mechanisms. A detailed  
 737 description of the  $tH$  mechanism will be given in section 2.4.

### 738 **2.3.7 Higgs boson decay channels**

739 When a particle can decay through several modes, also known as channels, the  
 740 probability of decaying through a given channel is quantified by the “branching ratio  
 741 (BR)” of the decay channel; thus, the BR is defined as the ratio of number of decays  
 742 going through that given channel to the total number of decays. In regard to the  
 743 Higgs boson decay, the BR can be predicted with accuracy once the Higgs mass is  
 744 known [37, 38]. In figure 2.12 right, a plot of the BR as a function of the Higgs mass  
 745 is presented. The largest predicted BR corresponds to the  $b\bar{b}$  pair decay channel (see  
 746 table 2.9).

Decay channel	Branching ratio	Rel. uncertainty
$H \rightarrow bb$	$5.84 \times 10^{-1}$	+3.2% – 3.3%
$H \rightarrow W^+W^-$	$2.14 \times 10^{-1}$	+4.3% – 4.2%
$H \rightarrow \tau^+\tau^-$	$6.27 \times 10^{-2}$	+5.7% – 5.7%
$H \rightarrow ZZ$	$2.62 \times 10^{-2}$	+4.3% – 4.1%
$H \rightarrow \gamma\gamma$	$2.27 \times 10^{-3}$	+5.0% – 4.9%
$H \rightarrow Z\gamma$	$1.53 \times 10^{-3}$	+9.0% – 8.9%
$H \rightarrow \mu^+\mu^-$	$2.18 \times 10^{-4}$	+6.0% – 5.9%

**Table 2.9:** Predicted branching ratios and the relative uncertainty for a SM Higgs boson with  $m_H = 125 GeV/c^2$ . [9]

## 748 2.4 Associated production of a Higgs boson and a 749 single Top quark.

750 Associated production of Higgs boson has been extensively studied [39–43]. While  
751 measurements of the main Higgs production mechanisms rates are sensitive to the  
752 strength of the Higgs coupling to W boson or top quark, they are not sensitive to the  
753 relative sign between the two couplings. In this thesis, the Higgs boson production  
754 mechanism explored is the associated production with a single top quark (*th*) which  
755 offers sensitiveness to the relative sign of the Higgs couplings to W boson and to top  
756 quark. The description given here is based on the reference [41]

757  
758 A process where two incoming particles interact and produce a final state with two  
759 particles can proceed in three ways also called channels (see, for instance, figure 2.13  
760 ommiting the red line). The t-channel represents processes where an intermediate  
761 particle is emitted by one of the incoming particles and absorbed by the other. The  
762 s-channel represents processes where the two incoming particles merge into an inter-  
763 mediate particle which eventually will split into the particles in the final state. The  
764 third channel, u-channel, is similar to the t-channel but the two outgoing particles

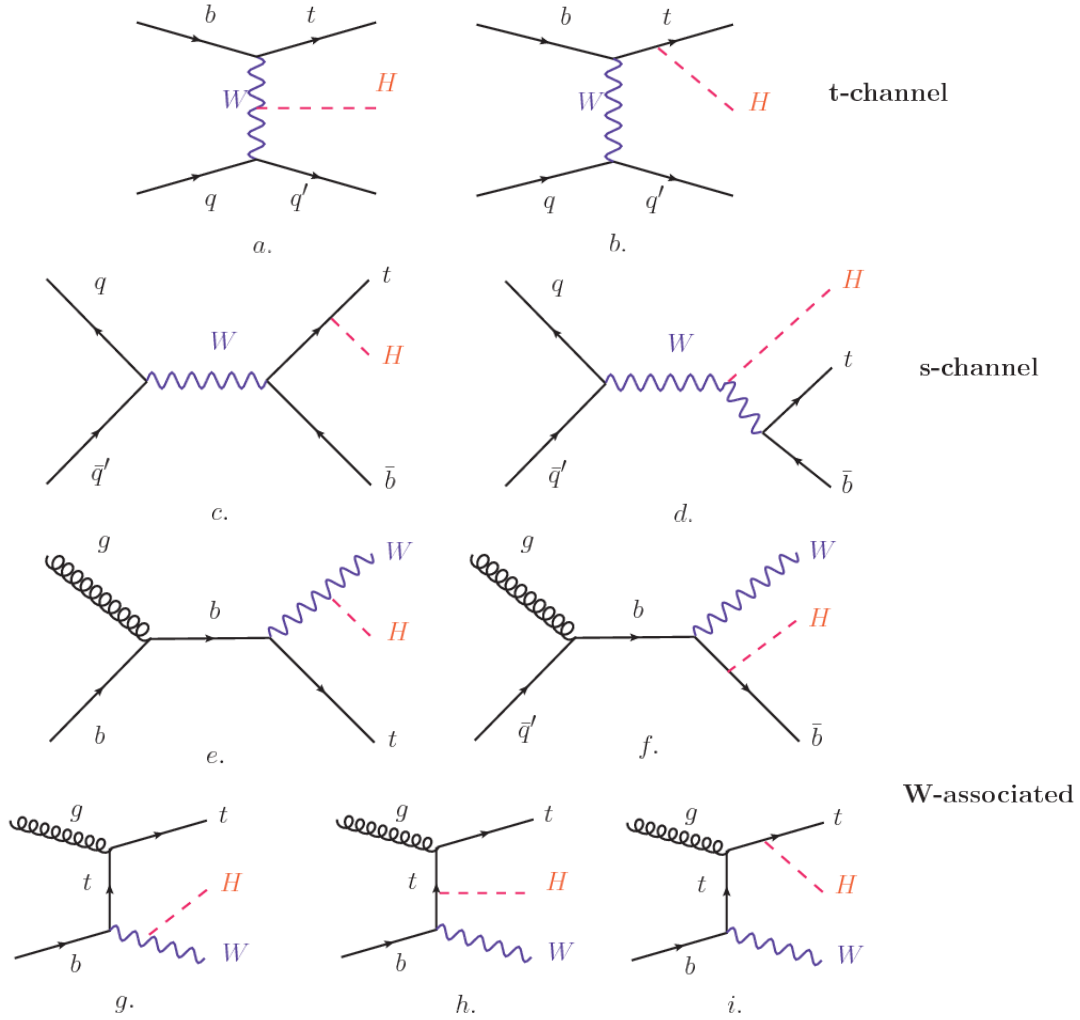


**Figure 2.13:** Associated Higgs boson production mechanism Feynman diagrams. a.,b. t-channel (tHq), c.,d. s-channel (tHb), e-i. W-associated.

765 interchange their roles.

766

767 The *th* production, where Higgs boson can be radiated either from the top quark or  
 768 from the W boson, is represented by the leading order Feynman diagrams in figure  
 769 2.13. The cross section for the *th* process is calculated, as usual, summing over  
 770 the contributions from the different feynman diagrams; therefore it depends on the  
 771 interference between the contributions. In the SM, the interference for t-channel (tHq

772 process) and W-associated (tHW process) production is destructive [39] resulting in  
 773 the small cross sections presented in table 2.10.

tH production channel	Cross section (fb)
t-channel ( $pp \rightarrow tHq$ )	$70.79^{+2.99}_{-4.80}$
W-associated ( $pp \rightarrow tHW$ )	$15.61^{+0.83}_{-1.04}$
s-channel( $pp \rightarrow tHb$ )	$2.87^{+0.09}_{-0.08}$

**Table 2.10:** Predicted SM cross sections for  $tH$  production at  $\sqrt{s} = 13$  TeV [44, 45].

774

775 While the s-channel contribution can be neglected, it will be shown that a deviation  
 776 from the SM destructive interference would result in an enhancement of the  $th$  cross  
 777 section compared to that in SM, which could be used to get information about the  
 778 sign of the Higgs-top coupling [41, 42]. In order to describe  $th$  production processes,  
 779 Feynman diagram 2.13b will be considered; there, the W boson is radiated by a  
 780 quark in the proton and eventually it will interact with the b quark. In the high  
 781 energy regime, the effective W approximation [46] allows to describe the process as  
 782 the emmision of an approximately on-shell W and its hard scattering with the b  
 783 quark; i.e.  $Wb \rightarrow th$ . The scattering amplitude for the process is given by

$$\mathcal{A} = \frac{g}{\sqrt{2}} \left[ (\kappa_t - \kappa_V) \frac{m_t \sqrt{s}}{m_W v} A \left( \frac{t}{s}, \varphi; \xi_t, \xi_b \right) + \left( \kappa_V \frac{2m_W s}{v} \frac{1}{t} + (2\kappa_t - \kappa_V) \frac{m_t^2}{m_W v} \right) B \left( \frac{t}{s}, \varphi; \xi_t, \xi_b \right) \right], \quad (2.57)$$

784 where  $\kappa_V \equiv g_{HVV}/g_{HVV}^{SM}$  and  $\kappa_t \equiv g_{Ht}/g_{Ht}^{SM} = y_t/y_t^{SM}$  are scaling factors that quan-  
 785 tify possible deviations of the couplings, Higgs-Vector boson (H-W) and Higgs-top  
 786 (H-t) respectively, from the SM couplings;  $s = (p_W + p_b)^2$ ,  $t = (p_W - p_H)^2$ ,  $\varphi$  is the  
 787 Higgs azimuthal angle around the  $z$  axis taken parallel to the direction of motion of  
 788 the incoming W; A and B are funtions describing the weak interaction in terms of

789 the chiral states of the quarks  $b$  and  $t$ . Terms that vanish in the high energy limit  
 790 have been neglected as well as the Higgs and  $b$  quark masses<sup>8</sup>.

791

792 The scattering amplitude grows with energy like  $\sqrt{s}$  for  $\kappa_V \neq \kappa_t$ , in contrast to  
 793 the SM ( $\kappa_t = \kappa_V = 1$ ), where the first term in 2.57 cancels out and the amplitude  
 794 is constant for large  $s$ ; therefore, a deviation from the SM predictions represents an  
 795 enhancement in the  $tHq$  cross section. In particular, for a SM H-W coupling and a H-t  
 796 coupling of inverted sign with respect to the SM ( $\kappa_V = -\kappa_t = 1$ ) the  $tHq$  cross section  
 797 is enhanced by a factor greater 10 as seen in the figure 2.14 taken from reference [41];  
 798 reference [47] has reported similar enhancement results.

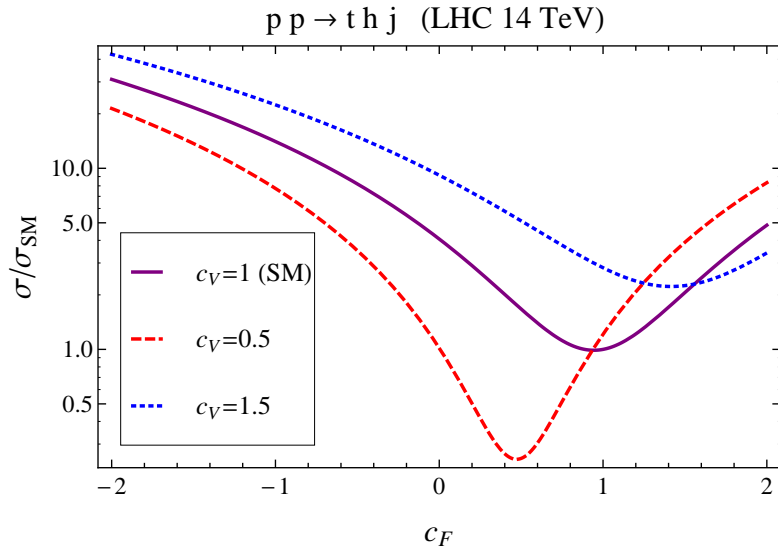


**Figure 2.14:** Cross section for  $tHq$  process as a function of  $\kappa_t$ , normalized to the SM, for three values of  $\kappa_V$ . In the plot  $c_f$  refers to the Higgs-fermion coupling which is dominated by the H-t coupling and represented here by  $\kappa_t$ . Solid, dashed and dotted lines correspond to  $c_V \rightarrow \kappa_V = 1, 0.5, 1.5$  respectively. Note that for the SM ( $\kappa_V = \kappa_t = 1$ ), the destructive effect of the interference is maximal.

799 A similar analysis is valid for the W-associated channel but, in that case, the inter-  
 800 ference is more complicated since there are more than two contributions and an ad-

---

<sup>8</sup> A detailed explanation of the structure and approximations used to derive  $\mathcal{A}$  can be found in reference [41]

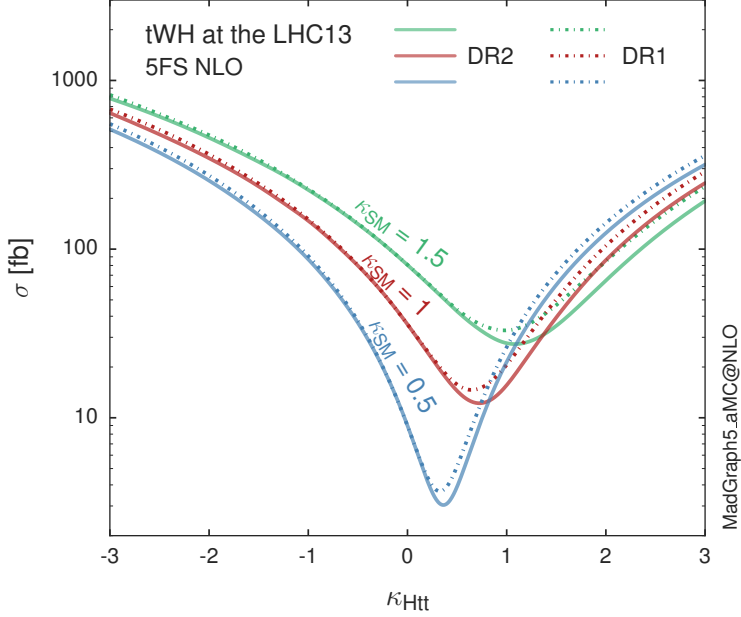


**Figure 2.15:** Cross section for  $tHW$  process as a function of  $\kappa_{Htt}$ , for three values of  $\kappa_{SM}$  at  $\sqrt{s} = 13$  TeV.  $\kappa_{Htt}^2 = \sigma_{Htt}/\sigma_{Htt}^{SM}$  is a simple rescaling of the SM Higgs interactions.

ditional interference with the production of Higgs boson and a top pair process( $t\bar{t}H$ ).  
The calculations are made using the so-called Diagram Removal (DR) technique where  
interfering diagrams are removed (or added) from the calculations in order to evaluate  
the impact of the removed contributions. DR1 was defined to neglect  $t\bar{t}H$  interference  
while DR2 was defined to take  $t\bar{t}H$  interference into account [48]. As shown in figure  
2.15, the  $tHW$  cross section is enhanced from about 15 fb (SM:  $\kappa_{Htt} = 1$ ) to about  
150 fb ( $\kappa_{Htt} = -1$ ). Differences between curves for DR1 and DR2 help to gauge the  
impact of the interference with  $t\bar{t}H$ .  
Results of the calculations of the  $tHq$  and  $tHW$  cross sections at  $\sqrt{s} = 13$  TeV can be  
found in reference [49] and a summary of the results is presented in table 2.11.

	$\sqrt{s}$ TeV	$\kappa_t = 1$	$\kappa_t = -1$
$\sigma^{LO}(tHq)(fb)$ [41]	8	$\approx 17.4$	$\approx 252.7$
	14	$\approx 80.4$	$\approx 1042$
$\sigma^{NLO}(tHq)(fb)$ [41]	8	$18.28^{+0.42}_{-0.38}$	$233.8^{+4.6}_{-0.0}$
	14	$88.2^{+1.7}_{-0.0}$	$982.8^{+28}_{-0.0}$
$\sigma^{LO}(tHq)(fb)$ [47]	14	$\approx 71.8$	$\approx 893$
$\sigma^{LO}(tHW)(fb)$ [47]	14	$\approx 16.0$	$\approx 139$
$\sigma^{NLO}(tHq)(fb)$ [49]	8	$18.69^{+8.62\%}_{-17.13\%}$	-
	13	$74.25^{+7.48\%}_{-15.35\%}$	$848^{+7.37\%}_{-13.70\%}$
	14	$90.10^{+7.34\%}_{-15.13\%}$	$1011^{+7.24\%}_{-13.39\%}$
$\sigma^{LO}(tHW)(fb)$ [48]	13	$15.77^{+15.91\%}_{-15.76\%}$	-
$\sigma^{NLO}DR1(tHW)(fb)$ [48]	13	$21.72^{+6.52\%}_{-5.24\%}$	$\approx 150$
$\sigma^{NLO}DR2(tHW)(fb)$ [48]	13	$16.28^{+7.34\%}_{-15.13\%}$	$\approx 150$

**Table 2.11:** Predicted enhancement of the  $tHq$  and  $tHW$  cross sections at LHC for  $\kappa_V = 1$  and  $\kappa_t = \pm 1$  at LO and NLO; the cross section enhancement of more than a factor of 10 is due to the flippling in the sign of the H-t coupling with respect to the SM one.

## 812 2.5 The CP-mixing in tH processes

813 In addition to the sensitivity to sign of the H-t coupling,  $tHq$  and  $tHW$  processes have  
 814 been proposed as a tool to investigate the possibility of a H-t coupling that does not  
 815 conserve CP [43, 48, 50]. Current experimental results are consistent with SM H-V  
 816 and H-t couplings; however, negative H-t coupling is not excluded completely [52].

817

818 In this thesis, the sensitivity of  $th$  processes to CP-mixing is also studied in the  
 819 effective field theory framework and based in references [43, 48]; a generic particle  
 820 ( $X_0$ ) of spin-0 and a general CP violating interaction with the top quark, can couple  
 821 to scalar and pseudoscalar fermionic densities. The H-W interaction is assumed to  
 822 be SM-like. The Lagrangian modeling the H-t interaction is given by

$$\mathcal{L}_0^t = -\bar{\psi}_t (c_\alpha \kappa_{Htt} g_{Htt} + i s_\alpha \kappa_{Att} g_{Att} \gamma_5) \psi_t X_0, \quad (2.58)$$

823 where  $\alpha$  is the CP-mixing phase,  $c_\alpha \equiv \cos \alpha$  and  $s_\alpha \equiv \sin \alpha$ ,  $\kappa_{Htt}$  and  $\kappa_{Att}$  are real  
 824 dimensionless rescaling parameters<sup>9</sup>,  $g_{Htt} = g_{Att} = m_t/v = y_t/\sqrt{2}$  and  $v \sim 246$  GeV is  
 825 the Higgs vacuum expectation value. In this parametrization, it is easy to recover  
 826 three special cases

- 827     • CP-even coupling  $\rightarrow \alpha = 0^\circ$
- 828     • CP-odd coupling  $\rightarrow \alpha = 90^\circ$
- 829     • SM coupling  $\rightarrow \alpha = 0^\circ$  and  $\kappa_{Htt} = 1$

830 The loop induced  $X_0$  coupling to gluons can also be described in terms of the  
 831 parametrization above, according to

$$\mathcal{L}_0^g = -\frac{1}{4} \left( c_\alpha \kappa_{Hgg} g_{Hgg} G_{\mu\nu}^a G^{a,\mu\nu} + s_\alpha \kappa_{Agg} g_{Agg} G_{\mu\nu}^a \tilde{G}^{a,\mu\nu} \right) X_0. \quad (2.59)$$

832 where  $g_{Hgg} = -\alpha_s/3\pi v$  and  $g_{Agg} = \alpha_s/2\pi v$ . Under the assumption that the top quark  
 833 dominates the gluon-fusion process at LHC energies,  $\kappa_{Hgg} \rightarrow \kappa_{Htt}$  and  $\kappa_{Agg} \rightarrow \kappa_{Att}$ ,  
 834 so that the ratio between the gluon-gluon fusion cross section for  $X_0$  and for the SM  
 835 Higgs prediction can be written as

$$\frac{\sigma_{NLO}^{gg \rightarrow X_0}}{\sigma_{NLO,SM}^{gg \rightarrow H}} = c_\alpha^2 \kappa_{Htt}^2 + s_\alpha^2 \left( \kappa_{Att} \frac{g_{Agg}}{g_{Hgg}} \right)^2. \quad (2.60)$$

836 If the rescaling parameters are set to

$$\kappa_{Htt} = 1, \quad \kappa_{Att} = \left| \frac{g_{Hgg}}{g_{Agg}} \right| = \frac{2}{3}. \quad (2.61)$$

837 the gluon-fusion SM cross section is reproduced for every value of the CP-mixing  
 838 angle  $\alpha$ ; therefore, by imposing that condition to the Lagrangian density 2.58, the

---

<sup>9</sup> analog to  $\kappa_t$  and  $\kappa_V$

CP-mixing angle is not constrained by current data. Figure 2.16 shows the NLO cross sections for t-channel  $tX_0$ (blue) and  $t\bar{t}X_0$  (red) associated production processes as a function of the CP-mixing angle  $\alpha$ .  $X_0$  is a generic spin-0 particle with top quark CP-violating coupling. Rescaling factors  $\kappa_{Htt}$  and  $\kappa_{Att}$  have been set to reproduce the SM gluon-fusion cross sections.

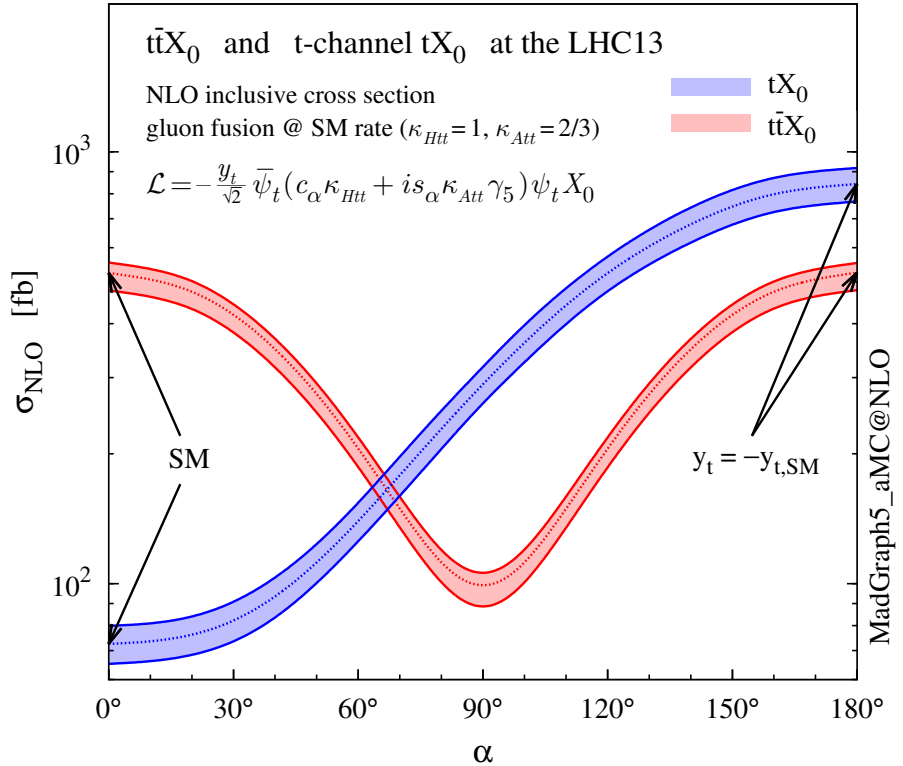


**Figure 2.16:** NLO cross sections for t-channel  $tX_0$ (blue) and  $t\bar{t}X_0$  (red) associated production processeses as a function of the CP-mixing angle  $\alpha$ .  $X_0$  is a generic spin-0 particle with top quark CP-violating coupling [43].

It is interesting to notice that the  $tX_0$  croos section is enhanced, by a factor of about 10, when a continuous rotation in the scalar-pseudoscalar plane is applied; this enhancement is similar to the enhancement produced when the H-t coupling is flipped in sign with respect to the SM ( $y_t = -y_{t,SM}$  in the plot), as showed in section 2.4. In contrast, the degeneracy in the  $t\bar{t}X_0$  cross section is still present given that it depends

quadratically on the H-t coupling, but more interesting is to notice that  $t\bar{t}X_0$  cross section is exceeded by  $tX_0$  cross section after  $\alpha \sim 60^\circ$ .

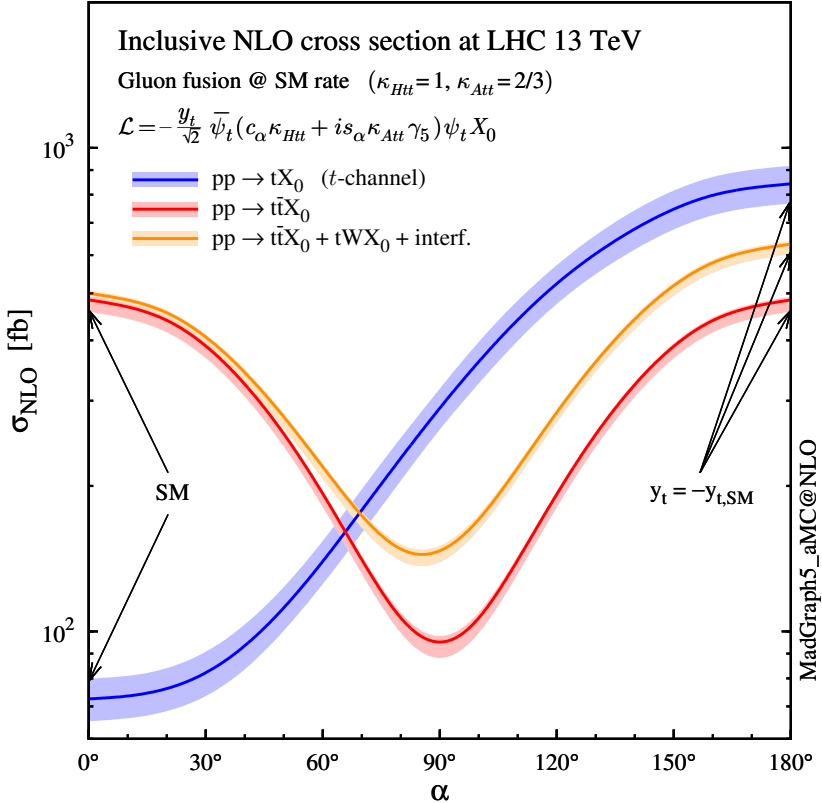


**Figure 2.17:** NLO cross sections for t-channel  $tX_0$ (blue),  $t\bar{t}X_0$  (red) associated production processes and combined  $tWX_0 + t\bar{t}X_0$  (including interference) production as a function of the CP-mixing angle  $\alpha$  [43].

850

851 A similar parametrization can be used to investigate the  $tHW$  process sensitivity to  
 852 CP-violating H-t coupling. As said in 2.4, the interference in the W-associated chan-  
 853 nel is more complicated because there are more than two contributions and also there  
 854 is interference with the  $t\bar{t}H$  production process.

855

856 Figure 2.17 shows the NLO cross sections for t-channel  $tX_0$ (blue),  $t\bar{t}X_0$  (red) asso-  
 857 ciated production and for the combined  $tWX_0 + t\bar{t}X_0 +$  interference (orange) as a  
 858 function of the CP-mixing angle. It is clear that the effect of the interference in the

combined case is the lifting of the degeneracy present in the  $t\bar{t}X_0$  production. The constructive interference enhances the cross section from about 500 fb at SM ( $\alpha = 0$ ) to about 600 fb ( $\alpha = 180^\circ \rightarrow y_t = -y_{t,SM}$ ).

An analysis combining  $tHq$  and  $tHW$  processes will be made in this thesis taking advantage of the sensitivity improvement.

## 2.6 Experimantal status of the anomalous Higg-fermion coupling.

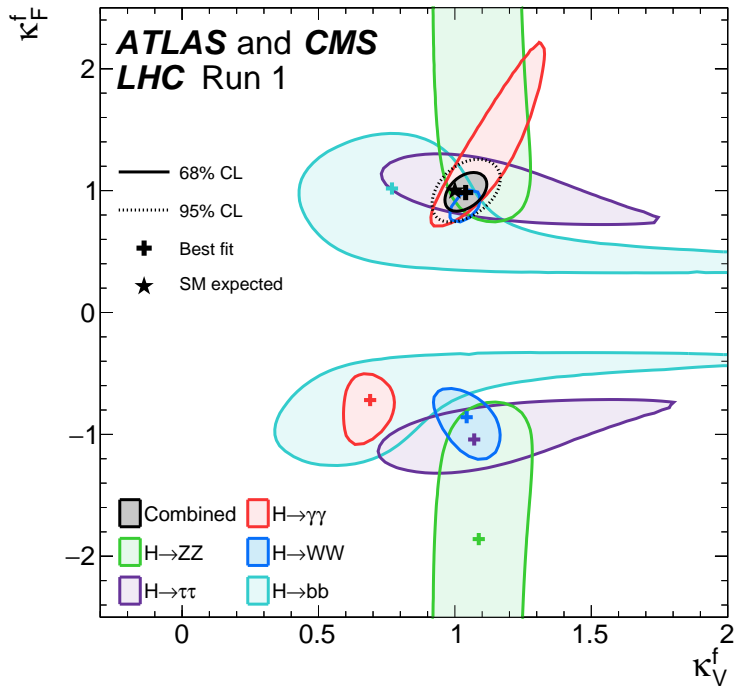


**Figure 2.18:** Combination of the ATLAS and CMS fits for coupling modifiers  $\kappa_t$ - $\kappa_V$ ; also shown the individual decay channels combination and their global combination. No assumptions have been made on the sign of the coupling modifiers [52].

ATLAS and CMS have performed analysis of the anomalous H-f coupling by making likelihood scans for the two coupling modifiers,  $\kappa_t$  and  $\kappa_V$ , under the assumption that

868  $\kappa_Z = \kappa_W = \kappa_V$  and  $\kappa_t = \kappa_\tau = \kappa_b = \kappa_f$ . Figure 2.18 shows the result of the combination  
869 of ATLAS and CMS fits; also the individual decay channels combination and the  
870 global combination results are shown.

871 While all the channels are compatible for positive values of the modifiers, for negative  
872 values of  $\kappa_t$  there is no compatibility. The best fit for individual channels is compatible  
873 with negative values of  $\kappa_t$  except for the  $H \rightarrow bb$  channel which is expected to be the  
874 most sensitive channel; therefore, the best fit for the global fit yields  $\kappa_t \geq 0$ . Thus,  
875 the anomalous H-t coupling cannot be excluded completely.

<sup>876</sup> **Chapter 3**

<sup>877</sup> **The CMS experiment at the LHC**

<sup>878</sup> **3.1 Introduction**

<sup>879</sup> Located on the Swiss-French border, the European Council for Nuclear Research  
<sup>880</sup> (CERN) is the largest scientific organization leading the particle physics research.  
<sup>881</sup> About 13000 people in a broad range of fields including users, students, scientists,  
<sup>882</sup> engineers among others, contribute to the data taking and analysis, with the goal  
<sup>883</sup> of unveiling the secrets of nature and revealing the fundamental structure of the  
<sup>884</sup> universe. CERN is also the home of the Large Hadron Collider (LHC), the largest  
<sup>885</sup> circular particle accelerator around the world, where protons (or heavy ions) traveling  
<sup>886</sup> close to the speed of light, are made to collide. These collisions open a window  
<sup>887</sup> to investigate how particles (and their constituents if they are composite) interact  
<sup>888</sup> with each other, providing clues about the laws of nature. This chapter presents an  
<sup>889</sup> overview of the LHC structure and operation. A detailed description of the CMS  
<sup>890</sup> detector is offered, given that the data used in this thesis have been taken with this  
<sup>891</sup> detector.

## 892 3.2 The LHC

893 With 27 km of circumference, the LHC is currently the largest and most powerful  
 894 circular accelerator in the world. It is installed in the same tunnel where the Large  
 895 Electron-Positron (LEP) collider was located, taking advantage of the existing infras-  
 896 tructure. The LHC is also the larger accelerator in the CERN's accelerator complex  
 897 and is assisted by several successive accelerating stages before the particles are in-  
 898 jected into the LHC ring where they reach their maximum energy (see figure 3.1).

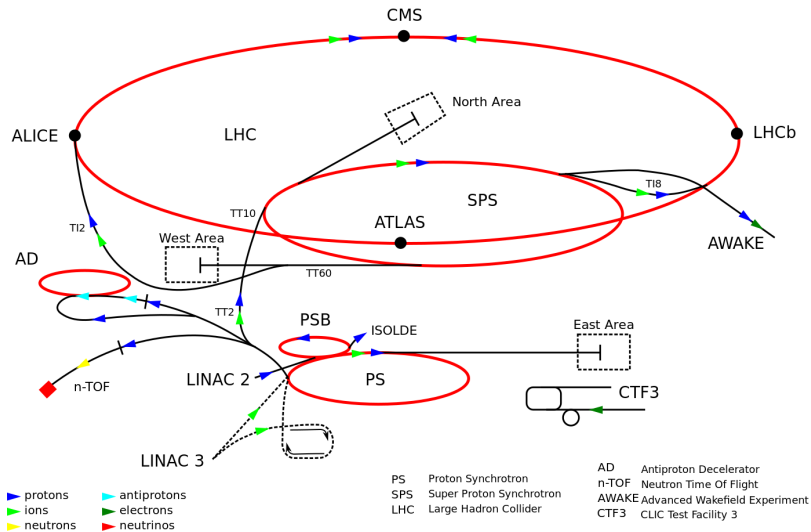


**Figure 3.1:** CERN accelerator complex. Blue arrows show the path followed by protons along the acceleration process [53].

899 LHC run in three modes depending on the particles being accelerated

- 900     • Proton-Proton collisions ( $p\bar{p}$ ) for multiple physics experiments.  
 901     • Lead-Lead collisions ( $Pb-Pb$ ) for heavy ion experiments.  
 902     • Proton-Lead collisions ( $p-Pb$ ) for quark-gluon plasma experiments.

903 In this thesis  $p\bar{p}$  collisions will be considered.

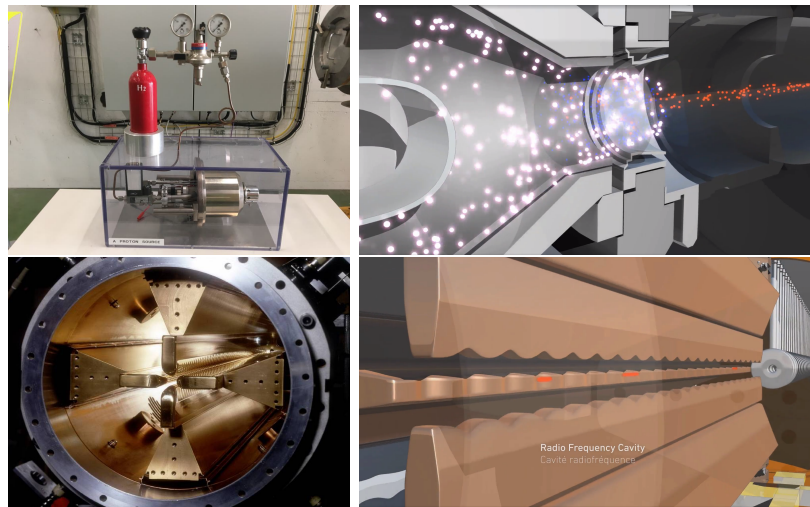


**Figure 3.2:** LHC protons source and the first acceleration stage. Top: the bottle contains hydrogen gas (white dots) which is injected into the metal cylinder to be broken down into electrons(blue dots) and protons(red dots); Bottom: the obtained protons are directed towards the radio frequency quadrupole which perform the first acceleration, focus the beam and create the bunches of protons. [57, 58]

905 Collection of protons starts with hydrogen atoms taken from a bottle, containing hy-  
 906 drogen gas, and injecting them in a metal cylinder; hydrogen atoms are broken down  
 907 into electrons and protons by an intense electric field (see figure3.2 top). The result-  
 908 ing protons leave the metal cylinder towards a radio frequency quadrupole (RFQ)  
 909 that focus the beam, accelerate the protons and create the packets of protons called  
 910 bunches. In the RFQ, an electric field is generated by a RF wave at a frequency that  
 911 matches the resonance frequency of the cavity where the electrodes are contained.  
 912 The beam of protons traveling on the RFQ axis experience an alternating electric  
 913 field gradient that generates the focusing forces.

914

915 In order to accelerate the protons, a longitudinal time-varying electric field component  
 916 is added to the system; it is done by giving the electrodes a sinus-like profile as shown  
 917 in figure 3.2 bottom. By matching the speed and phase of the protons with the  
 918 longitudinal electric field the bunching is performed; protons synchronized with the

919 RFQ (synchronous proton) does not feel an accelerating force, but those protons in  
 920 the beam that have more (or less) energy than the synchronous proton (asynchronous  
 921 protons) will feel a decelerating (accelerating) force; therefore, asynchronous protons  
 922 will oscillate around the synchronous ones forming bunches of protons [55]. From the  
 923 RFQ emerges protons with energy 750 keV in bunches of about  $1.15 \times 10^{11}$  protons  
 924 [56].

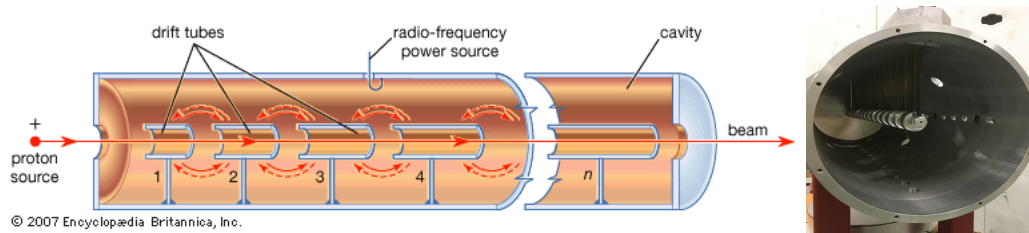


**Figure 3.3:** The LINAC2 accelerating system at CERN. Radio frequency (RF) generated electric fields create acceleration and deceleration zones inside the cavity; deceleration zones are blocked by drift tubes where quadrupole magnets focus the proton beam. [59]

925 Proton bunches coming from the RFQ goes to the linear accelerator 2 (LINAC2)  
 926 where they are accelerated to reach 50 MeV energy. In the LINAC2 stage, acceler-  
 927 ation is performed using radio frequency generated electric fields which create zones  
 928 of acceleration and deceleration as shown in figure 3.3. In the decelerations zones,  
 929 the electric field is blocked using drift tubes where protons are free to drift while  
 930 quadrupole magnets focus the beam.

931

932 The beam coming from LINAC2 is injected into the proton synchrotron booster  
 933 (PSB) to reach 1.4 GeV in energy. The next acceleration is provided at the pro-  
 934 ton synchrotron (PS) up to 26 GeV, followed by the injection into the super proton  
 935 synchrotron (SPS) where protons are accelerated to 450 GeV. Finally, protons are  
 936 injected into the LHC where they are accelerated to the target energy of 6.5 TeV.  
 937 PSB, PS, SPS and LHC accelerate protons using the same RF acceleration technic

described before.

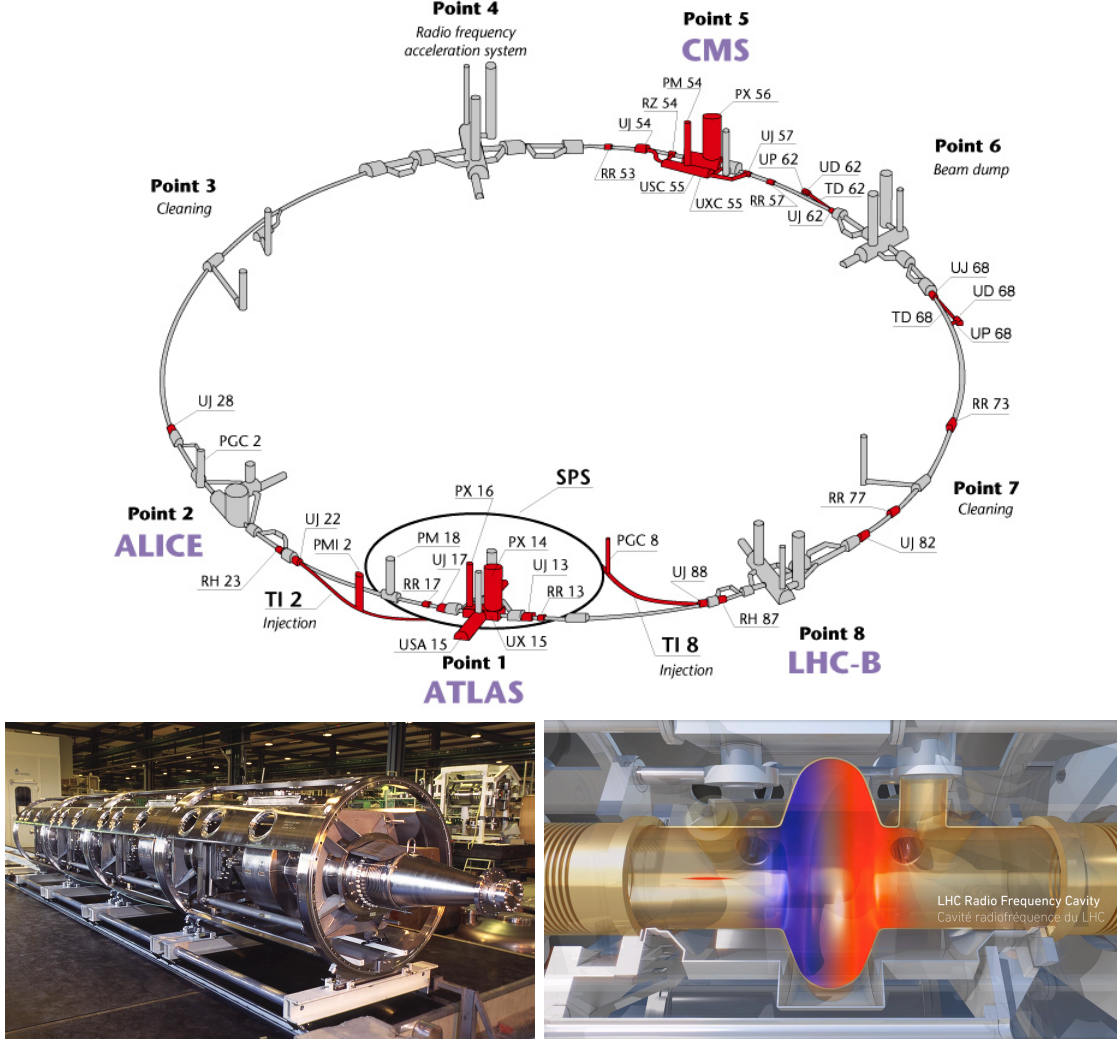


**Figure 3.4:** Top: LHC layout. The red zones indicate the infrastructure additions to the LEP installations, built to accomodate the ATLAS and CMS experiments which exceed the size of the former experiments located there [54]. Bottom: LHC RF cavities. A module accomodates 4 cavities that accelerate protons and preserve the bunch structure of the beam. [58, 60]

LHC has a system of 16 RF cavities located in the so-called point 4, as shown in figure 3.4 top, tunned at a frequency of 400 MHz and the protons are carefully timed so in addition to the acceleration effect the bunch structure of the beam is preserved. Bottom side of figure 3.4 shows a picture of a Rf module composed of 4 RF cavities

943 working in a superconducting state at 4.5 K; also is showed a representation of the  
 944 accelerating electric field that accelerates the protons in the bunch.

945

946 While protons are accelerated in one section of the LHC ring, where the RF cavities  
 947 are located, in the rest of their path they have to be kept in the curved trajectory  
 948 defined by the LHC ring. Technically, LHC is not a perfect circle; RF, injection, beam  
 949 dumping, beam cleaning and sections before and after the experimental points where  
 950 protons collide are all straight sections. In total, there are 8 arcs 2.45 Km long each  
 951 and 8 straight sections 545 m long each. In order to curve the proton's trajectory in  
 952 the arc sections, superconducting dipole magnets are used.

953

954 Inside the LHC ring, there are two proton beams traveling in opposite directions in  
 955 two separated beam pipes; the beam pipes are kept at ultra-high vacuum ( $\sim 10^{-9}$   
 956 Pa) to ensure that there are no particles that interact with the proton beams. The  
 957 superconducting dipole magnets used in LHC are made of a NbTi alloy, capable of  
 958 transporting currents of about 12000 A when cooled at a temperature below 2K using  
 959 liquid helium (see figure 3.5).

960 Protons in the arc sections of LHC feel a centripetal force exerted by the dipole  
 961 magnets which is perpendicular to the beam trajectory; The magnitude of magnetic  
 962 field needed can be found assuming that protons travel at  $v \approx c$ , using the standard  
 963 values for proton mass and charge and the LHC radius, as

$$F_m = \frac{mv^2}{r} = qBv \quad \rightarrow B = 8.33T \quad (3.1)$$

964 which is about 100000 times the Earth's magnetic field. A representation of the  
 965 magnetic field generated by the dipole magnets is shown in the bottom left side of

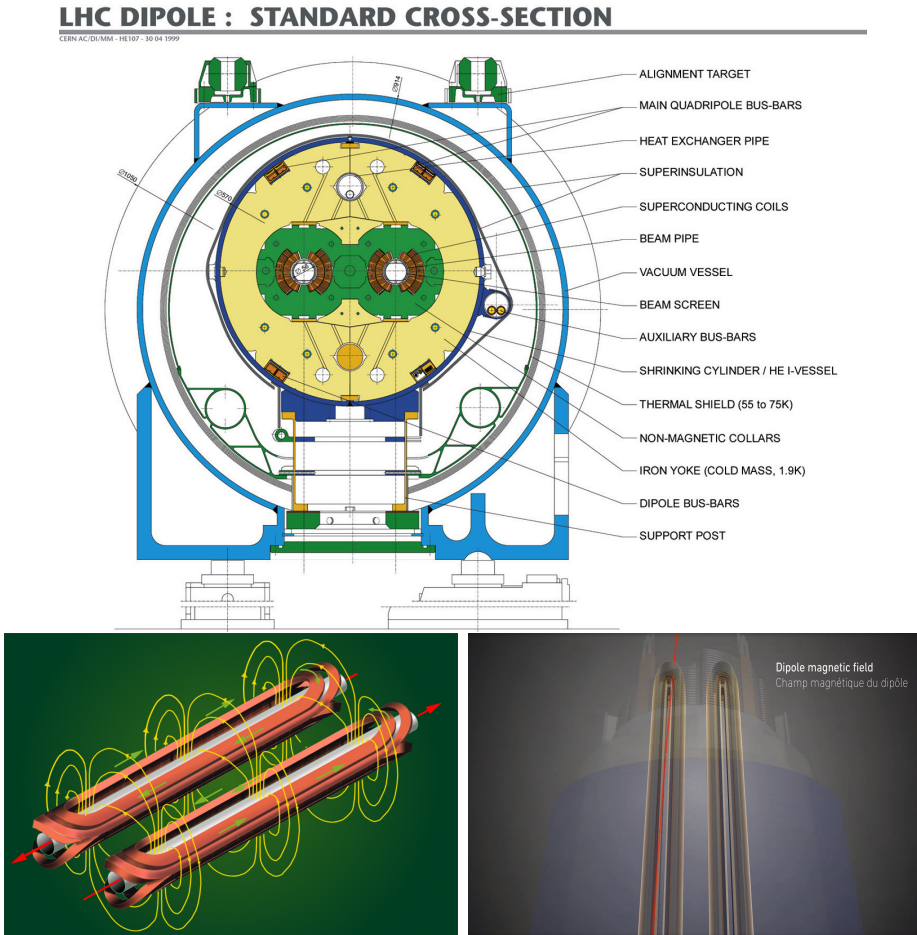


**Figure 3.5:** Top: LHC dipole magnet transversal view; cooling, shielding and mechanical support are indicated. Bottom left: Magnetic field generated by the dipole magnets; note that the direction of the field inside one beam pipe is opposite with respect to the other beam pipe which guarantee that both proton beams are curved in the same direction towards the center of the ring. The effect of the dipole magnetic field on the proton beam is represented in the bottom right side [58, 61, 62].

966 figure 3.5. The bending effect of the magnetic field on the proton beam is shown in  
 967 the bottom right side of figure 3.5. Note that the dipole magnets are not curved; the  
 968 arc section of the LHC ring is composed of straight dipole magnets of about 15 m.  
 969 In total there are 1232 dipole magnets along the LHC ring.  
 970 In addition to bending the beam trajectory, the beam has to be focused so it stays  
 971 inside the beam pipe. The focusing is performed by quadrupole magnets installed

972 in another straight section; in total 858 quadrupole magnets are installed along the  
 973 LHC ring. Other effects like electromagnetic interaction among bunches, interaction  
 974 with electron clouds from the beam pipe, the gravitational force on the protons,  
 975 differences in energy among protons in the same bunch, among others, are corrected  
 976 using sextupole and other magnetic multipoles.

977 The two proton beams inside the LHC ring are made of bunches with a cylindrical  
 978 shape of about 7.5 cm long and about 1 mm in diameter; when bunches are close  
 979 to the collision point (CP), the beam is focused up to a diameter of about 16  $\mu\text{m}$   
 980 in order to maximize the luminosity ( $L$ ) defined as the number of collisions per unit  
 981 area and per second. Luminosity can be calculated using

$$L = fn \frac{N_1 N_2}{4\pi\sigma_x\sigma_y} \quad (3.2)$$

982 where  $f$  is the revolution frequency,  $n$  is the number of bunches per beam,  $N_1$  and  $N_2$   
 983 are the numbers of protons per bunch,  $\sigma_x$  and  $\sigma_y$  are the gaussian transverse sizes of  
 984 the bunches. Using

$$f = \frac{v}{2\pi r_{LHC}} \approx \frac{3 \times 10^8 \text{ m/s}}{27 \text{ km}} \approx 11.1 \text{ kHz},$$

$$n = 2808$$

$$N_1 = N_2 = 1.5 \times 10^{11}$$

$$\sigma_x = \sigma_y = 16 \mu\text{m}$$

985

$$L = 1.28 \times 10^{34} \text{ cm}^{-2} \text{ s}^{-1} \quad (3.3)$$

986 Luminosity is a fundamental aspect for LHC given that the bigger luminosity, the  
 987 bigger number of collisions, which means that for processes with a very small cross

section the number of expected occurrences is increased and so the chances of being detected. The integrated luminosity collected by the CMS experiment during 2016 is shown in figure 3.6; the data analyzed in this thesis corresponds to an integrated luminosity of  $35.9 \text{ fb}^{-1}$  at  $\sqrt{s} = 13 \text{ TeV}$ .

A way to increase L is increasing the number of bunches in the beam. Currently, the separation between two consecutive bunches in the beam is 7.5 m which corresponds to a time separation of 25 ns. In the full LHC ring the allowed number of bunches is  $n = 27\text{km}/7.5\text{m} = 3600$ ; however, there are some gaps in the bunch pattern intended for preparing the dumping and injection of the beam, thus, the proton beams are composed of 2808 bunches.

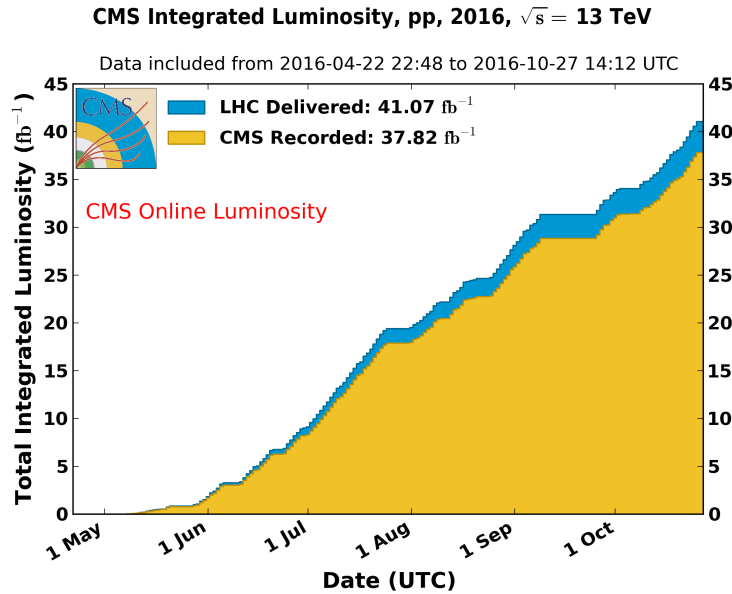


**Figure 3.6:** Integrated luminosity delivered by LHC and recorded by CMS during 2016. The difference between the delivered and the recorded luminosities is due to fails and issues occurred during the data taking in the CMS experiment [63].

Once the proton beams reach the desired energy, they are brought to cross each other producing proton-proton collisions. The bunch crossing happens in precise places where the four LHC experiments are located, as seen in figure 3.7 left. In 2008, the

1001 first set of collisions involved protons with  $\sqrt{s} = 7$  TeV; the energy was increased to  
 1002 8 TeV in 2012 and to 13 TeV in 2015.

1003 CMS and ATLAS experiments, which are multi-purpose experiments, are enabled  
 1004 to explore physics in any of the collision modes. LHCb experiment is optimized  
 1005 to explore bottom quark physics, while ALICE is optimized for heavy ion collisions  
 1006 searches; TOTEM and LHCf are dedicated to forward physics studies; MoEDAL (not  
 1007 indicated in the figure) is intended for monopoles or massive pseudo stable particles  
 1008 searches.

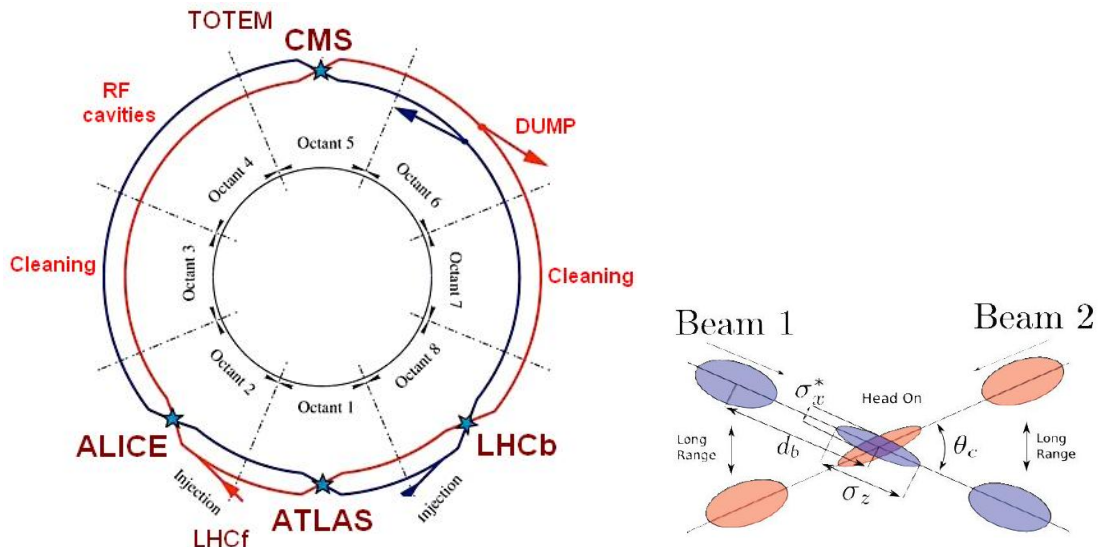


**Figure 3.7:** Left: LHC interaction points. Bunch crossing occurs where the LHC experiments are located [64]. Sections indicated as cleaning are dedicated to collimate the beam in order to protect the LHC ring from collisions with protons in very spreaded bunches. Right: bunch crossing scheme. Since the bunch crossing is not perfectly head-on, the luminosity is reduced in a factor of 17%.

1009 At the CP there are two interesting details that need to be addressed. The first  
 1010 one is that the bunch crossing does not occur head-on but at a small crossing angle  
 1011 (280  $\mu$ rad in CMS and ATLAS) as shown in the right side of figure 3.7, affecting the  
 1012 overlapping between bunches; the consequence is a reduction of about 17% in the  
 1013 luminosity. The second one is the occurrence of multiple pp collisions in the same

1014 bunch crossing; this effect is called pile-up (PU). A fairly simple estimation of the  
 1015 PU follows from estimating the probability of collision between two protons, one from  
 1016 each of the bunches in course of collision; it depends roughly on the ratio of proton  
 1017 size and the cross section of the bunch in the interaction point, i.e.,

$$P(pp\text{-}collision) \sim \frac{d_{proton}^2}{\sigma_x \sigma_y} = \frac{(1fm)^2}{(16\mu m)^2} \sim 4 \times 10^{-21} \quad (3.4)$$

1018 however, there are  $N = 1.15 \times 10^{11}$  protons in a bunch, thus the estimated number of  
 1019 collisions in a bunch crossing is

$$PU = N^2 * P(pp\text{-}collision) \sim 50 \text{ pp-collision per bunch crossing}, \quad (3.5)$$

1020 about 20 of those pp collisions are inelastic. Each collision generates a vertex, but  
 1021 only the most energetic is considered as a primary vertex; the rest are considered as  
 1022 PU vertices. A multiple pp collision event in a bunch crossing at CMS is showed in  
 1023 figure3.8. Unstable particles outgoing from the primary vertex will eventually decay;  
 1024 this decay vertex is known as a secondary vertex.

1025 on

1026 Next section presents a description of the CMS detector which it is the detector used  
 1027 to collect the data used in this thesis.

### 1028 3.3 The CMS experiment

1029 CMS is a general-purpose detector designed to conduct research in a wide range  
 1030 of physics from the standard model to new physics like extra dimensions and dark  
 1031 matter. Located at the point 5 in the LHC layout as shown in figure 3.4, CMS is

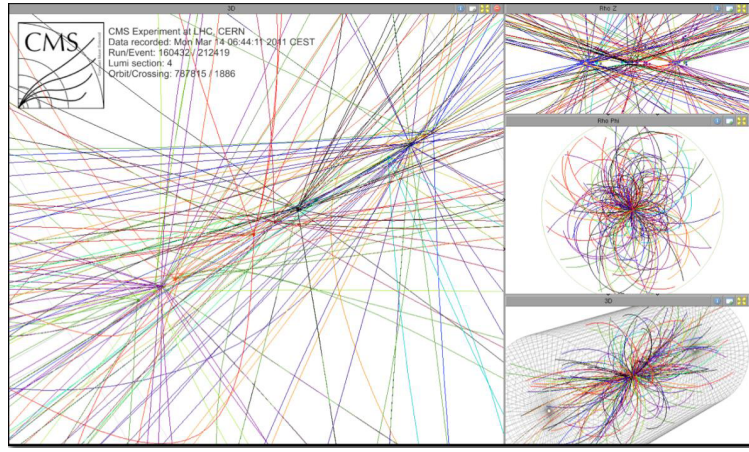


**Figure 3.8:** Multiple pp collision bunch crossing at CMS. Only the most energetic vertex is considered and the rets are cataloged as PU vertices [].

1032 composed of several detection systems distributed in a cylindrical structure; in total,  
 1033 CMS weights about 12500 tons in a very compact 21.6 m long and 14.6 m diameter  
 1034 cylinder. It was built in 15 separate sections at the ground level and lowered to the  
 1035 cavern individually to be assembled. A complete and detailed description of the CMS  
 1036 detector and its components is given in reference [65] on which this section is based in.  
 1037

1038 Figure 3.9 shows the layout of the CMS detector. The design is driven by the require-  
 1039 ments on the identification, momentum resolution and unambiguous charge determi-  
 1040 nation of the muons; therefore, a large bending power is provided by the solenoid  
 1041 magnet made of superconducting cable capable to generate a 3.8 T magnetic field.  
 1042 The detection system is composed of (from the innermost to the outermost)

- 1043     • Pixel detector.
- 1044     • Silicon strip tracker.
- 1045     • Preshower detector.
- 1046     • Electromagnetic calorimeter.

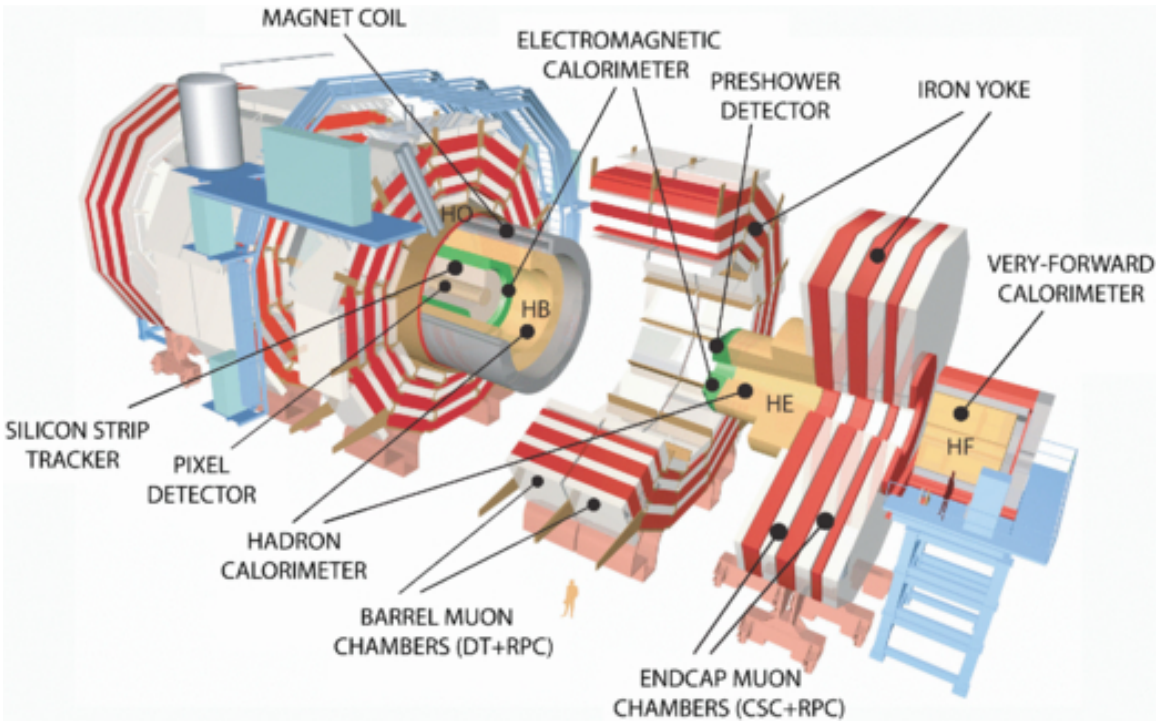


**Figure 3.9:** Layout of the CMS detector. The several subdetectors are indicated. The central region of the detector is referred as the Barrel section while the endcaps are referred as the forward sections. [66].

1047 • Hadronic calorimeter.

1048 • Muon chambers (Barrel and endcap)

1049 The central region of the detector is commonly referred as the barrel section while the  
 1050 endcaps are referred as the forward sections of the detector; thus, each subdetector  
 1051 is composed of a barrel section and a forward section.

### 1052 **3.3.1 Coordinate system**

1053 The coordinate system used by CMS is centered in the geometrical center of the  
 1054 detector which is the same as the CP as shown in figure 3.10. The  $z$ -axis is parallel  
 1055 to the beam direction, while the  $Y$ -axis pointing vertically upward, and the  $X$ -axis  
 1056 pointing radially inward toward the center of the LHC.

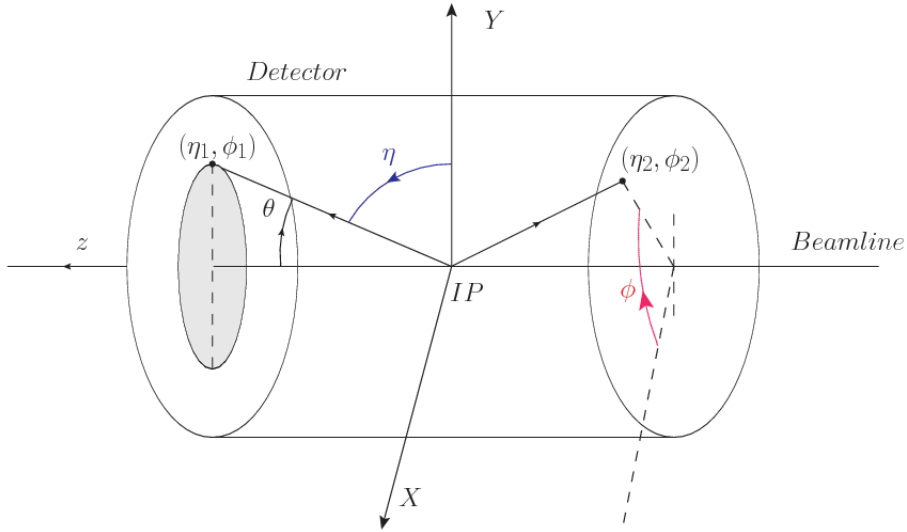


**Figure 3.10:** CMS detector coordinate system.

1057 In addition to the common cartesian and cylindrical coordinate systems, two coordi-  
 1058 nates are of particular utility in particle physics: rapidity( $y$ ) and pseudorapidity( $\eta$ ),  
 1059 defined in connection to the polar angle  $\theta$ , energy and longitudinal momentum com-  
 1060 ponent (momentum along the  $z$ -axis) according to

$$y = \frac{1}{2} \ln \frac{E + p_z}{E - p_z} \quad \eta = -\ln \left( \tan \frac{\theta}{2} \right) \quad (3.6)$$

1061 Rapidity is related to the angle between the  $XY$ -plane and the direction in which the  
 1062 products of a collision are emitted; it has the nice property that the difference between  
 1063 the rapidities of two particles is invariant with respect to Lorentz boosts along the  $z$ -  
 1064 axis. Thus, data analysis becomes more simple when based on rapidity; however, it is  
 1065 not simple to measure the rapidity of highly relativistic particles, as those produced  
 1066 after pp collisions. Under the highly relativistic motion approximation,  $y$  can be  
 1067 rewritten in terms of the polar angle, concluding that rapidity is approximately equal  
 1068 to the pseudorapidity defined above, i.e.  $y \approx \eta$ . Note that  $\eta$  is easier to measure than  $y$   
 1069 given the direct relationship between the former and the polar angle. Angular distance

1070 between two objects in the detector ( $\Delta R$ ) is defined in terms of their coordinates  
 1071  $(\eta_1, \phi_1), (\eta_2, \phi_2)$  as

$$\Delta R = \sqrt{(\Delta\eta)^2 - (\Delta\phi)^2} \quad (3.7)$$

1072 **3.3.2 Pixels detector**

1073 The CMS tracking system is designed to provide a precise measurement of the tra-  
 1074 jectory followed by the charged particles created after the pp collisions as; also, the  
 1075 precise reconstruction of the primary and secondary vertices is expected in an envi-  
 1076 ronment where, each 25 ns, the bunch crossing produce about 20 inelastic collisions  
 1077 and about 1000 particles. An increment in the luminosity is ongoing which implies  
 1078 that the PU will increase accordingly.

1079

1080 The pixel detector was replaced during the 2016-2017 year end shut down, due to the  
 1081 increasingly challenging operating conditions like the higher particle flow and more  
 1082 radiation harsh environment among others. The new one is responding as expected,  
 1083 reinforcing its crucial role in the successful way to fulfill the new LHC physics ob-  
 1084 jectives after the discovery of the Higgs boson. The last chapter of this thesis is  
 1085 dedicated to describe my contribution to the “Forward Pixel Phase 1 upgrade”.

1086

1087 The current pixel detector is composed of 1856 silicon pixel detector modules orga-  
 1088 nized in four-barrel layers in the central region and three disks in the forward region;  
 1089 it is designed to record efficiently and with high precision, up to  $10\mu\text{m}$  in the  $XY$ -  
 1090 plane and  $20\mu\text{m}$  in the  $z$ -direction, the first four space-points near to the CP region  
 1091 (see figure 3.11 left side) in the range  $|\eta| \leq 2.5$ . The first barrel layer is located at a  
 1092 radius of 30 mm from the beamline, while the fourth layer is located at a radius of

1093 160 mm closer to the strip tracker inner barrel layer (see section 3.3.3) in order to  
 1094 reduce the rate of fake tracks. The high granularity of the detector is represented in  
 1095 its about 123 Mpixels, each of size  $100 \times 150 \mu\text{m}^2$ , which is almost twice the channels  
 1096 of the old detector. The transverse momentum resolution of tracks can be measured  
 1097 with a resolution of 1-2% for muons of  $p_T = 100 \text{ GeV}$ .

1098

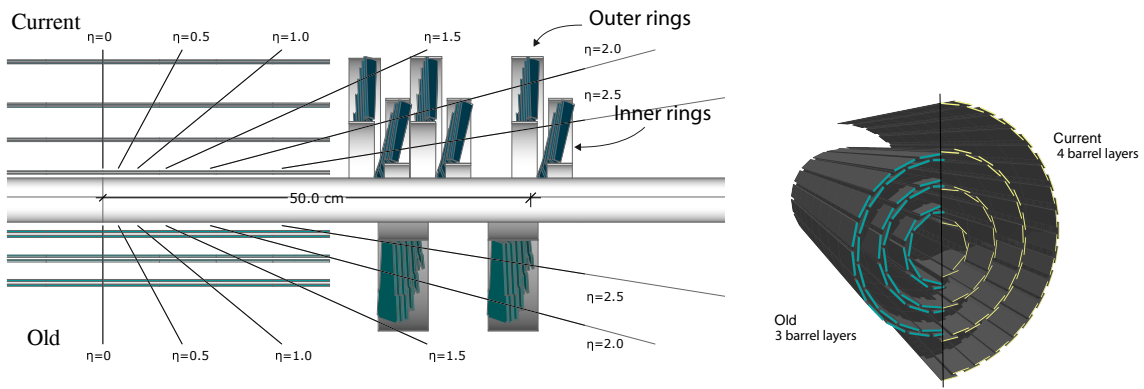


**Figure 3.11:** CMS pixel detector schematic view. Left: layout comparing the layers and disks in the old and current pixel detectors. Right: Transverse-oblique view comparing the pixel barrel layers in the two [68].

1099 Some of the improvements with respect to the previous pixel detector include a higher  
 1100 average tracking efficiency and lower average fake rate as well as higher track impact  
 1101 parameter resolution which is fundamental in order to increase the efficiency in the  
 1102 identification of jets originating from b quarks (b-tagging). A significant source of  
 1103 improvement comes from the overall reduction in the material budget of the detector  
 1104 which results in fewer photon conversions and less multiple scattering from charged  
 1105 particles.

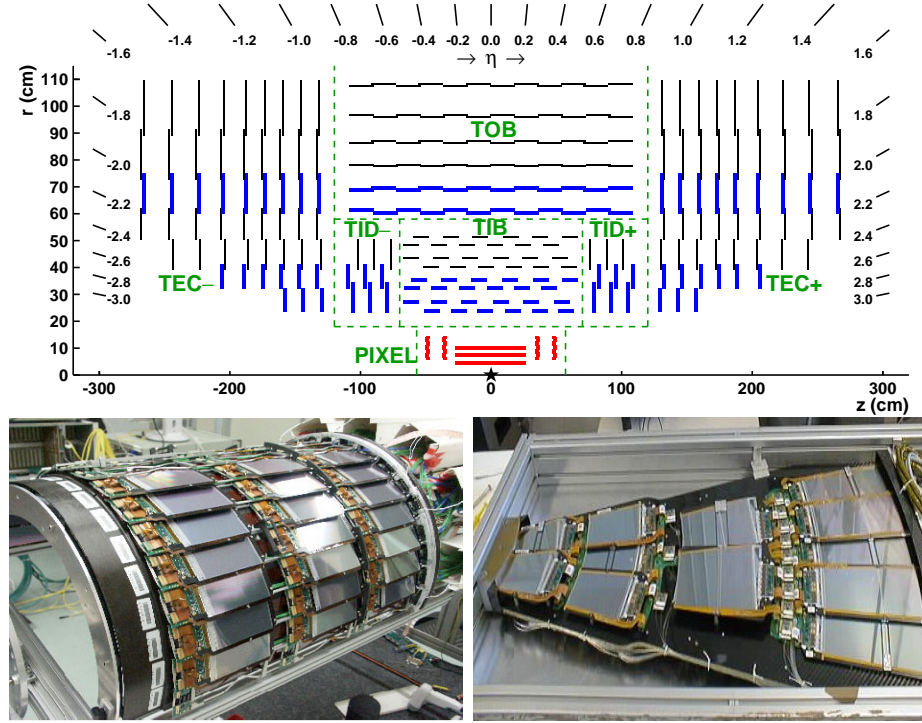


**Figure 3.12:** Top: CMS Silicon Strip Tracker (SST) schematic view. The SST is composed of the tracker inner barrel (TIB), the tracker inner disks (TID), the tracker outer barrel (TOB) and the tracker endcaps (TEC). Each part is made of silicon strip modules; the modules in blue represent two modules mounted back-to-back and rotated in the plane of the module by a stereo angle of 120 mrad in order to provide a 3-D reconstruction of the hit positions. Bottom: pictures of the TIB (left) and TEC (right) modules [69–71].

### 1106 3.3.3 Silicon strip tracker

1107 The silicon strip tracker (SST) is the second stage in the CMS tracking system. The  
 1108 top side of figure 3.12 shows a schematic of the SST. The inner tracker region is com-  
 1109 posed of the tracker inner barrel (TIB) and the tracker inner disks (TID) covering the  
 1110 region  $r < 55$  cm and  $|z| < 118$  cm. The TIB is composed of 4 layers while the TID  
 1111 is composed of 3 disks at each end. The silicon sensors in the inner tracker are 320  
 1112  $\mu\text{m}$  thick, providing a resolution of about 13–38  $\mu\text{m}$  in the  $r\phi$  position measurement.  
 1113  
 1114 The modules indicated in blue in the schematic view of figure 3.12 are two modules

1115 mounted back-to-back and rotated in the plane of the module by a “stereo” angle of  
 1116 100 mrad; the hits from these two modules, known as “stereo hits”, are combined to  
 1117 provide a measurement of the second coordinate ( $z$  in the barrel and  $r$  on the disks)  
 1118 allowing the reconstruction of hit positions in 3-D.

1119

1120 The outer tracker region is composed of the tracker outer barrel (TOB) and the  
 1121 tracker endcaps (TEC). The 6 layers of the TOB offers coverage in the region  $r > 55$   
 1122 cm and  $|z| < 118$  cm, while the 9 disks of the TEC cover the region  $124 < |z| < 282$   
 1123 cm. The resolution offered by the outer tracker is about 13-38  $\mu\text{m}$  in the  $r\phi$  position  
 1124 measurement. The inner four TEC disks use silicon sensors 320  $\mu\text{m}$  thick; those in  
 1125 the TOB and the outer three TEC disks use silicon sensors of 500  $\mu\text{m}$  thickness. The  
 1126 silicon strips run parallel to the  $z$ -axis and the distance between strips varies from 80  
 1127  $\mu\text{m}$  in the inner TIB layers to 183  $\mu\text{m}$  in the inner TOB layers; in the endcaps the  
 1128 wedge-shaped sensors with radial strips, whose pitch range between 81  $\mu\text{m}$  at small  
 1129 radii and 205  $\mu\text{m}$  at large radii.

1130

1131 The whole SST has 15148 silicon modules, 9.3 million silicon strips and cover a total  
 1132 active area of about 198  $\text{m}^2$

### 1133 3.3.4 Electromagnetic calorimeter

1134 The CMS electromagnetic calorimeter (ECAL) is designed to measure the energy of  
 1135 electrons and photons. It is composed of 75848 lead tungstate crystals which have a  
 1136 short radiation length (0.89 cm) and fast response, since 80% of the light is emitted  
 1137 within 25 ns; however, they are combined with Avalanche photodiodes (APDs) as  
 1138 photodetectors given that crystals themselves have a low light yield ( $30\gamma/\text{MeV}$ ). A

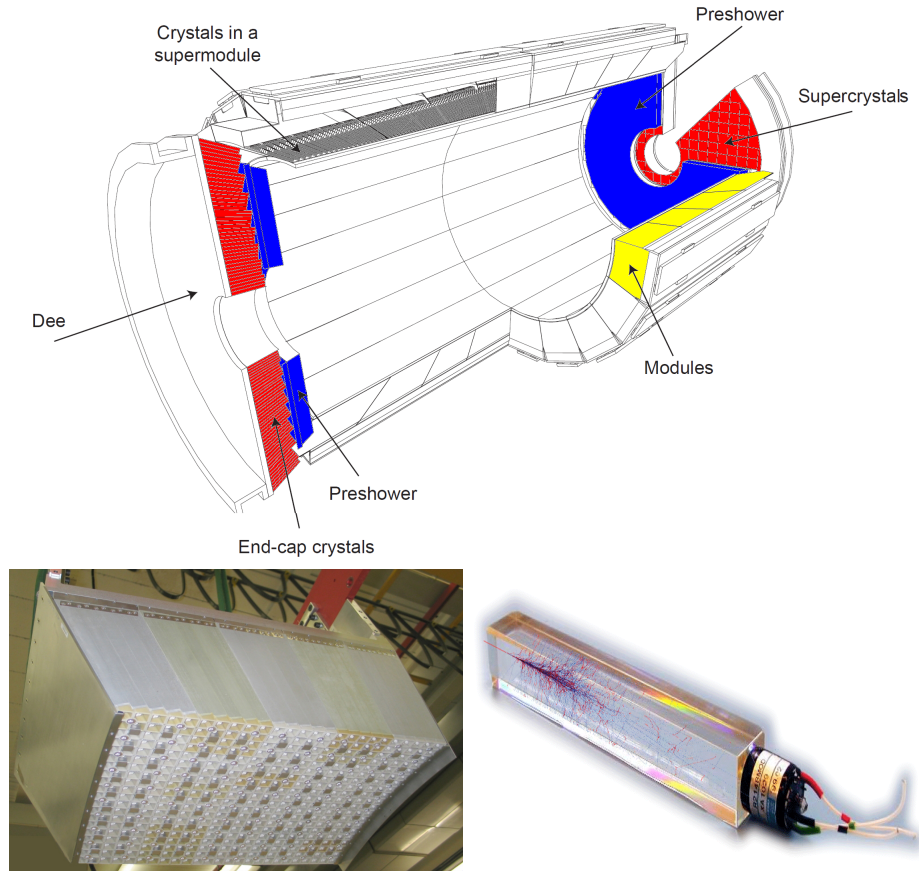


**Figure 3.13:** Top: CMS ECAL schematic view. Bottom: Module equipped with the crystals (left); ECAL crystal(right).

1139 schematic view of the ECAL is shown in figure 3.13.

1140

1141 Energy is measured by absorbing electrons and photons which generates an elec-  
 1142 tromagnetic “shower”, as seen in bottom right picture of the figure3.13. The ECAL  
 1143 barrel (EB) cover the region  $|\eta| < 1.479$ , using crystals of depth of 23 cm and  $2.2 \times 2.2$   
 1144  $\text{cm}^2$  transverse section.

1145 The ECAL endcap (EE) cover the region  $1.479 < |\eta| < 3.0$  using crystals of depth  
 1146 22 cm and transverse section of  $2.86 \times 2.86 \text{ cm}^2$ ; the photodetectors used are vacuum  
 1147 phototriodes (VPTs). Each EE is divided in two structures called “Dees”.

1148

1149 In front of the EE, it is installed the preshower detector (ES) which covers the region  
 1150  $1.653 < |\eta| < 2.6$ . The ES provides a precise measurement of the position of electro-  
 1151 magnetic showers, which allows to distinguish electrons and photons signals from  $\pi^0$   
 1152 decay signals. The ES is composed of a layer of lead absorber followed by a layer of  
 1153 plastic scintillators

1154 **3.3.5 Hadronic calorimeter**

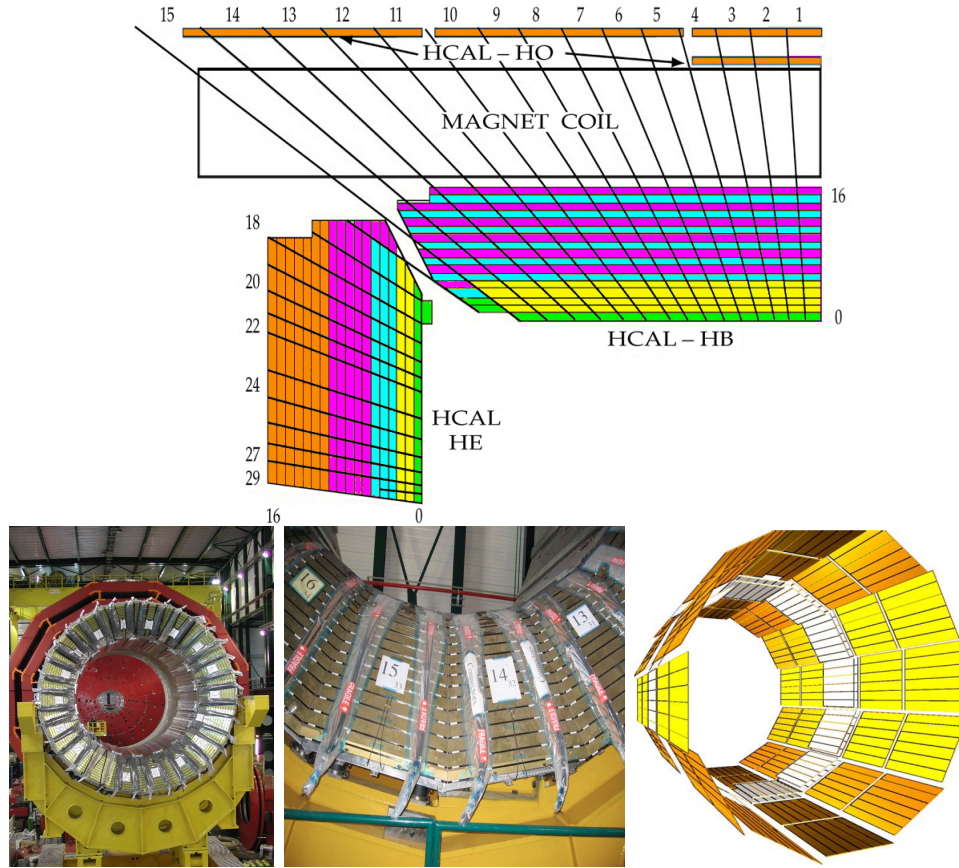


**Figure 3.14:** Top: CMS HCAL schematic view, the colors indicate the layers that are grouped into the same readout channels. Bottom: picture of a section of the HB; the absorber material is the golden region and scintillators are placed in between the absorber material (left and center). Schematic view of the HO (right). [72, 73]

1155 Hadrons are not absorbed by the ECAL but by the hadron calorimeter (HCAL),  
 1156 which is made of a combination of alternating brass absorber and silicon photo-  
 1157 multiplier(SiPM) layers; therefore, particles passing through the scintillator material  
 1158 produce showers, as in the ECAL, as a result of the inelastic scattering of the hadrons  
 1159 with the detector material. Since the particles are not absorbed in the scintillator,  
 1160 their energy is sampled; therefore the total energy is not measured but estimated,  
 1161 which reduce the resolution of the detector. Brass was chosen as the absorber mate-  
 1162 rial due to its short interaction length ( $\lambda_I = 16.42\text{cm}$ ) and its non-magnetivity. Figure  
 1163 3.14 shows a schematic view of the CMS HCAL.

1164

1165 The HCAL is divided into four sections; the Hadron Barrel (HB), the Hadron Outer  
 1166 (HO), the Hadron Endcap (HE) and the Hadron Forward (HF) sections. The HB  
 1167 cover the region  $0 < |\eta| < 1.4$ , while the HE covers the region  $1.3 < |\eta| < 3.0$ . The HF,  
 1168 made of quartz fiber scintillator and steel as absorption material, covers the forward  
 1169 region  $3.0 < |\eta| < 5.2$ . Both the HB and HF are located inside the solenoid. The HO  
 1170 is placed outside the magnet as an additional layer of scintillators with the purpose  
 1171 of measure the energy tails of particles passing through the HB and the magnet  
 1172 (see figure 3.14 top and bottom right). The upgrades made to the HCAL during  
 1173 the technical stop 2016-2017 consisted in the replacement of the photo transducer,  
 1174 improving the efficiency.

### 1175 3.3.6 Superconducting solenoid magnet

1176 The superconducting magnet installed is the CMS detector is designed to provide an  
 1177 intense and highly uniform magnetic field in the central part of the detector. In fact,  
 1178 the tracking system takes advantage of the bending power of the magnetic field to

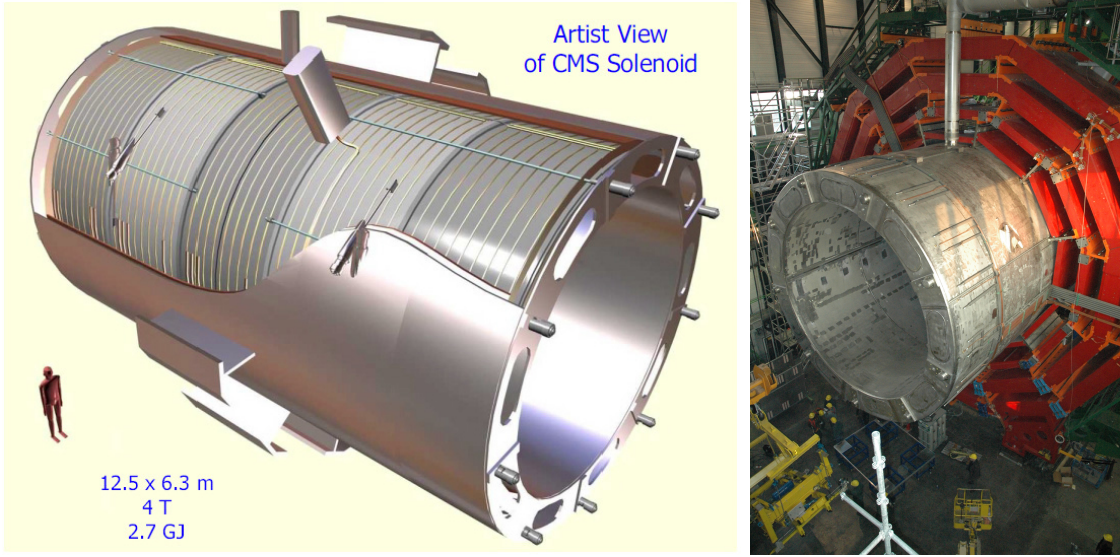


**Figure 3.15:** Artistic representation of the CMS solenoid magnet(left). The magnet is supported on an iron yoke (right) which also serves as the house of the muon detector and as mechanical support for the whole CMS detector [67].

1179 measure with precision the momentum of the particles that traverse it; the unam-  
 1180 biguous determination of the sign for high momentum muons was a driven principle  
 1181 during the design of the magnet. The magnet has a diameter of 6.3 m, a length of  
 1182 12.5 m and a cold mass of 220 t; the generated magnetic field reach a strength of 3.8T.  
 1183 Since it is made of Ni-Tb superconducting cable it has to operate at a temperature  
 1184 of 4.7 K by using a helium cryogenic system; the current circulating in the cables  
 1185 reach 18800 A under normal running conditions. The left side of figure 3.15 shows  
 1186 an artistic view of the CMS magnet, while the right side shows a transverse view of  
 1187 the cold mass where the winding structure is visible.

1188  
 1189 The yoke (see figure 3.15), composed of 5 barrel wheels and 6 endcap disks made  
 1190 of iron, serves not only as the media for magnetic flux return but also provides the  
 1191 house for the muon detector system and structural stability to the full detector.

1192 **3.3.7 Muon system**

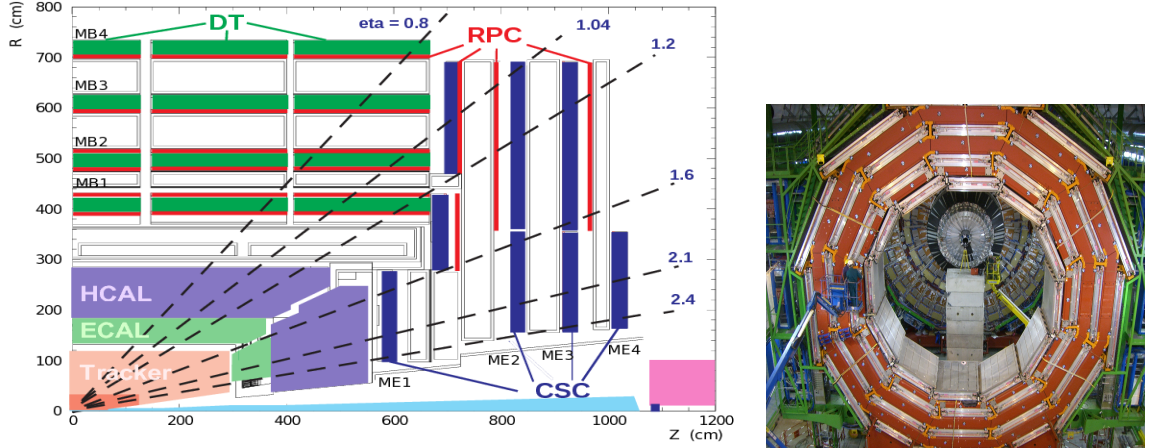


**Figure 3.16:** Left: CMS muon system schematic view; Right: one of the yoke rings with the muon DTs and RPCs installed; in the back it is possible to see the muon endcap [74].

1193 Muons are the only charged particles able pass through all the CMS detector due to  
 1194 their low ionization energy loss; thus, muons can be separated easily from the high  
 1195 amount of particles produced in a pp collision. Also, muons are expected to be pro-  
 1196 duced in the decay of several new particles; therefore, a good detection of muons was  
 1197 on the leading principles when designing the CMS detector.

1198

1199 The CMS muon detection system is embedded in the return yoke as seen in figure  
 1200 3.16. It is composed of three different detector types; the drift tube chambers (DT)  
 1201 are located in the central region  $\eta < 1.2$  arranged in four layers of drift chambers filled  
 1202 with an Ar/CO<sub>2</sub> gas mixture.

1203

1204 The muon endcaps are made of Cathode strip chambers (CSC) covering the region  
 1205  $\eta < 2.4$  and filled with a mixture of Ar/CO<sub>2</sub>/CF<sub>4</sub>. The reason behind using a different  
 1206 detector type lies on the different conditions in the forward region like the high muon  
 1207 rate and high residual magnetic field.

1208

1209 The third type of detector used in the muon system is a set four disks of resistive  
 1210 plate chambers (RPC) working in avalanche mode. The RPCs provide good spatial  
 1211 and time resolutions. The track of  $high - p_T$  muon candidate is built combining  
 1212 information from the tracking system and the signal from up to 6 RPCs and 4 DT  
 1213 chambers.

1214 **3.3.8 CMS trigger system**

1215 Under normal conditions, CMS expects pp collisions every 25 ns i.e. an interaction  
 1216 rate of 40 MHz for which it is not possible to store the recorded data in full. In order  
 1217 to handle this high event rate data, an online event selection, known as triggering, is  
 1218 performed; triggering reduce the event rate to 100 Hz for storage and further offline  
 1219 analysis.

1220

1221 The trigger system starts with a reduction of the event rate to 100 kHz in the so-called  
 1222 “level 1 trigger (L1)”. L1 is based on dedicated programmable hardware like Field  
 1223 Programmable Gate Arrays (FPGAs) and Application Specific Integrated Circuits  
 1224 (ASICs), partly located in the detector itself; another portion is located in the CMS  
 1225 under-ground cavern. Hit patterns information from the muon chambers and the  
 1226 energy deposits in the calorimeter are used to decide if an event is accepted or rejected,  
 1227 according to selection requirements previously defined which reflect the interesting  
 1228 physics processes. Figure 3.17 shows the L1 trigger architecture

1229 The second stage in the trigger system is called “ high-level trigger (HLT)”; events  
 1230 accepted by L1 are passed to HLT in order to make an initial reconstruction of them.  
 1231 HLT is software based and runs on a dedicated server farm, using selection algo-

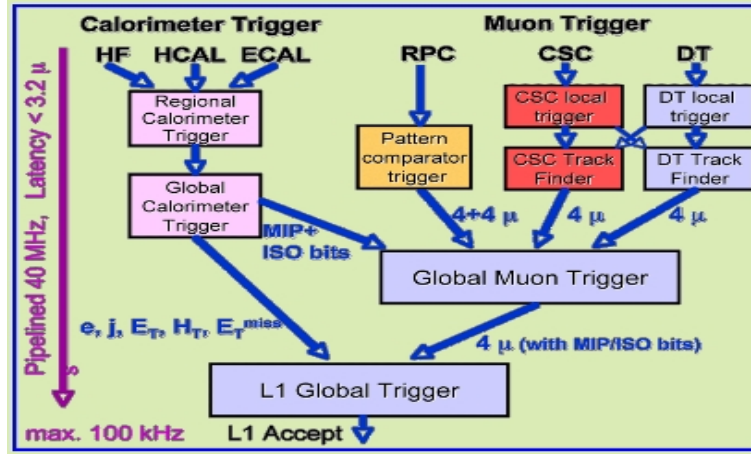


Figure 3.17: CMS Level-1 trigger architecture [75].

1232 rithms and high-level object definitions; the event rate at HLT is reduced to 100 Hz.  
 1233 The first HLT stage takes information from the muon detectors and the calorimeters  
 1234 to make the initial object reconstruction; in the next HLT stage, information from  
 1235 the pixel and strip detectors is used to do first fast-tracking and then full tracking  
 1236 online. This initial object reconstruction is used in further steps of the trigger system.

1237

1238 Events and preliminary reconstructed physics objects from HLT are sent to be fully  
 1239 reconstructed at the CERN computing center. Again, the pixel detector information  
 1240 provides high-quality seeds for the track reconstruction algorithm offline, primary ver-  
 1241 tex reconstruction, electron and photon identification, muon reconstruction,  $\tau$  iden-  
 1242 tification, and b-tagging. After full reconstruction, data sets are made available for  
 1243 offline analyses.

1244

1245 During the 2016-2017 technical stop, the L1 system was updated in order to improve  
 1246 the physics object identification by improving the algorithms and accounting for the  
 1247 increasing pile-up scenario.

### 1248 3.3.9 CMS computing

1249 After the data, coming from the experiment, are processed at several levels, they have  
 1250 to be stored and made available for further analysis; in order to cope all the tasks  
 1251 implied in the offline data processing, like transfer, simulation, reconstruction and  
 1252 reprocessing, among others, a big computing power is required. The CMS computing  
 1253 system is based on the distributed architecture concept, where users of the system  
 1254 and physical computer centers are distributed worldwide and interconnected by high-  
 1255 speed networks.

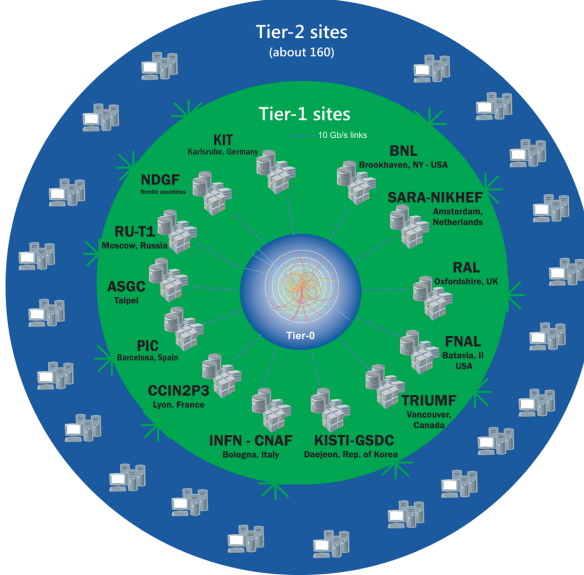


**Figure 3.18:** WLCG structure. The primary computer centers (Tier-0) are located at CERN (data center) and at the Wigner datacenter in Budapest. Tier-1 is composed of 13 centers and Tier-2 is composed of about 160 centers. [76].

1256 The worldwide LHC computing grid (WLCG) is the mechanism used to provide that  
 1257 distributed environment. WLCG is a tiered structure connecting computing centers  
 1258 around the world, which provide the necessary storage and computing facilities. The  
 1259 primary computing centers of the WLCG are located at the CERN and the Wigner  
 1260 datacenter in Budapest and are known as Tier-0 as shown in figure 3.18. The main

1261 responsibilities for each tier level are [76]

1262 • **Tier-0:** initial reconstruction of recorded events and storage of the resulting  
1263 datasets, the distribution of raw data to the Tier-1 centers.

1264 • **Tier-1:** provide storage capacity, support for the Grid, safe-keeping of a pro-  
1265 portional share of raw and reconstructed data, large-scale reprocessing and safe-  
1266 keeping of corresponding output, generation of simulated events, distribution  
1267 of data to Tier 2s, safe-keeping of a share of simulated data produced at these  
1268 Tier 2s.

1269 • **Tier-2:** store sufficient data and provide adequate computing power for specific  
1270 analysis tasks, provide analysis requirements and proportional share of simu-  
1271 lated event production and reconstruction.

1272 Aside from the general computing strategy to manage the huge amount of data pro-  
1273 duced by experiments, CMS uses a framework to perform a variety of processing,  
1274 selection and analysis tasks. The central concept of the CMS data model is the  
1275 “Event”; therefore, an event is the unit that contains the information from a single  
1276 bunch crossing as well as any data derived from that information like the recon-  
1277 structed objects, the details under which additional data are derived.

1278

1279 Events are passed as the input to the “physics modules” that obtain information from  
1280 them and create new one; for instance, “event data producers” add new data into the  
1281 events, “analyzers” produce an information summary from an event set, “filters” per-  
1282 form selection and triggering.

1283

1284 CMS uses several event formats with different levels of detail and precision

- 1285     • **Raw format:** events in this format contain the full recorded information from  
1286           the detector as well as trigger decision and other metadata. An extended version  
1287           of raw data is used to store information from the CMS Monte Carlo simulation  
1288           tools. Raw data are stored permanently, occupying about 2MB/event
- 1289     • **RECO format:** events in this format correspond to raw data that have been  
1290           submitted to reconstruction algorithms like primary and secondary vertex re-  
1291           construction, particle ID, track-finding. RECO events contain physical objects  
1292           and all the information used to reconstruct them; average size is about 0.5  
1293           MB/event.
- 1294     • **AOD format:** Analysis Object Data (AOD) is the data format used in the  
1295           physics analyses given that it contains the parameters describing the high-level  
1296           physics objects in addition to enough information to allow a kinematic refitting if  
1297           needed. AOD events are filtered versions of the RECO events to which skimming  
1298           or other kind processes have been applied. Requires about 100 kB/event.
- 1299     • **Non-event data** are data needed to interpret and reconstruct events. Some  
1300           of the non-event data used by CMS contains information about the detector  
1301           contraction and condition data like calibrations, alignment, and detector status.

1302     Figure 3.19 shows the data flow scheme between CMS detector and hardware tiers.

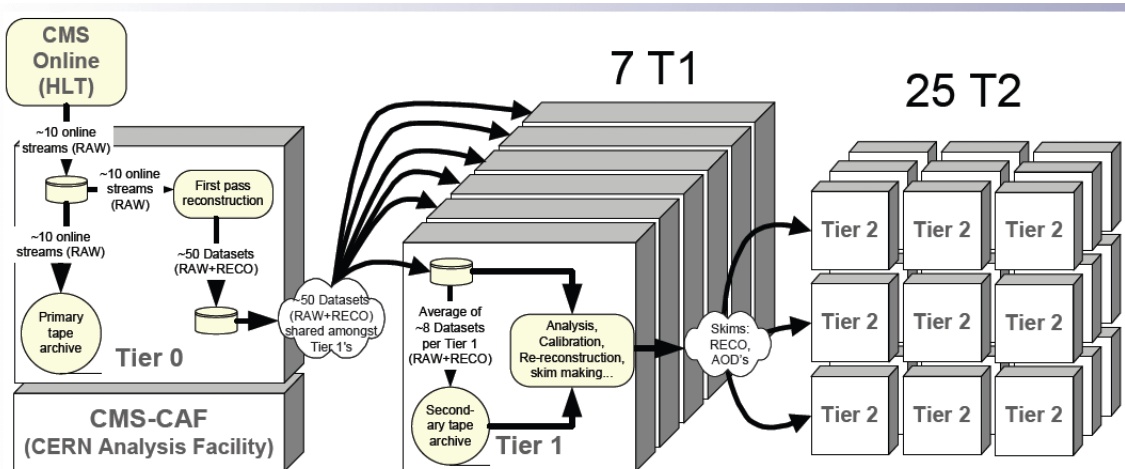


**Figure 3.19:** Data flow from CMS detector through hardware Tiers.

1303 **References**

- 1304 [1] J. Schwinger. “Quantum Electrodynamics. I. A Covariant Formulation”. Phys-  
1305       ical Review. 74 (10): 1439-61, (1948).
- 1306 [2] R. P. Feynman. “Space-Time Approach to Quantum Electrodynamics”. Physical  
1307       Review. 76 (6): 769-89, (1949).
- 1308 [3] S. Tomonaga. “On a Relativistically Invariant Formulation of the Quantum  
1309       Theory of Wave Fields”. Progress of Theoretical Physics. 1 (2): 27-42, (1946).
- 1310 [4] D.J. Griffiths, “Introduction to electrodynamics”. 4th ed. Pearson, (2013).
- 1311 [5] F. Mandl, G. Shaw. “Quantum field theory.” Chichester: Wiley (2009).
- 1312 [6] F. Halzen, and A.D. Martin, “Quarks and leptons: An introductory course in  
1313       modern particle physics”. New York: Wiley, (1984) .
- 1314 [7] File: Standard\_Model\_of\_Elementary\_Particle\_dark.svg. (2017, June 12)  
1315       Wikimedia Commons, the free media repository. Retrieved November  
1316       27, 2017 from <https://www.collegiate-advanced-electricity.com/single-post/2017/04/10/The-Standard-Model-of-Particle-Physics>.
- 1318 [8] E. Noether, “Invariante Variationsprobleme”, Nachrichten von der Gesellschaft  
1319       der Wissenschaften zu Göttingen, mathematisch-physikalische Klasse, vol. 1918,  
1320       pp. 235-257, (1918).

- 1321 [9] C. Patrignani et al. (Particle Data Group), Chin. Phys. C, 40, 100001 (2016)  
1322 and 2017 update.
- 1323 [10] M. Goldhaber, L. Grodzins, A.W. Sunyar “Helicity of Neutrinos”, Phys. Rev.  
1324 109, 1015 (1958).
- 1325 [11] Palanque-Delabrouille N et al. “Neutrino masses and cosmology with Lyman-  
1326 alpha forest power spectrum”, JCAP 11 011 (2015).
- 1327 [12] M. Gell-Mann. “A Schematic Model of Baryons and Mesons”. Physics Letters.  
1328 8 (3): 214-215 (1964).
- 1329 [13] G. Zweig. “An SU(3) Model for Strong Interaction Symmetry and its Breaking”  
1330 (PDF). CERN Report No.8182/TH.401 (1964).
- 1331 [14] G. Zweig. “An SU(3) Model for Strong Interaction Symmetry and its Breaking:  
1332 II” (PDF). CERN Report No.8419/TH.412(1964).
- 1333 [15] M. Gell-Mann. “The Interpretation of the New Particles as Displaced Charged  
1334 Multiplets”. Il Nuovo Cimento 4: 848. (1956).
- 1335 [16] T. Nakano, K, Nishijima. “Charge Independence for V-particles”. Progress of  
1336 Theoretical Physics 10 (5): 581-582. (1953).
- 1337 [17] N. Cabibbo, “Unitary symmetry and leptonic decays” Physical Review Letters,  
1338 vol. 10, no. 12, p. 531, (1963).
- 1339 [18] M.Kobayashi, T.Maskawa, “CP-violation in the renormalizable theory of weak  
1340 interaction,” Progress of Theoretical Physics, vol. 49, no. 2, pp. 652-657, (1973).
- 1341 [19] File: Weak Decay (flipped).svg. (2017, June 12). Wikimedia Com-  
1342 mons, the free media repository. Retrieved November 27, 2017 from

- 1343 https://commons.wikimedia.org/w/index.php?title=File:Weak\_Decay\_(flipped)  
1344 .svg&oldid=247498592.
- 1345 [20] Georgia Tech University. Coupling Constants for the Fundamental  
1346 Forces(2005). Retrieved January 10, 2018, from http://hyperphysics.phy-  
1347 astr.gsu.edu/hbase/Forces/couple.html#c2
- 1348 [21] M. Strassler. (May 31, 2013).The Strengths of the Known Forces. Retrieved Jan-  
1349 uary 10, 2018, from https://profmattstrassler.com/articles-and-posts/particle-  
1350 physics-basics/the-known-forces-of-nature/the-strength-of-the-known-forces/
- 1351 [22] S.L. Glashow. “Partial symmetries of weak interactions”, Nucl. Phys. 22 579-  
1352 588, (1961).
- 1353 [23] A. Salam, J.C. Ward. “Electromagnetic and weak interactions”, Physics Letters  
1354 13 168-171, (1964).
- 1355 [24] S. Weinberg, “A model of leptons”, Physical Review Letters, vol. 19, no. 21, p.  
1356 1264, (1967).
- 1357 [25] M. Peskin, D. Schroeder, “An introduction to quantum field theory”. Perseus  
1358 Books Publishing L.L.C., (1995).
- 1359 [26] A. Pich. “The Standard Model of Electroweak Interactions”  
1360 https://arxiv.org/abs/1201.0537
- 1361 [27] F.Bellaiche. (2012, 2 September). “What’s this Higgs boson anyway?”. Retrieved  
1362 from: https://www.quantum-bits.org/?p=233
- 1363 [28] M. Endres et al. Nature 487, 454-458 (2012) doi:10.1038/nature11255

- 1364 [29] F. Englert, R. Brout. “Broken Symmetry and the Mass of Gauge  
 1365 Vector Mesons”. Physical Review Letters. 13 (9): 321-23.(1964)  
 1366 doi:10.1103/PhysRevLett.13.321
- 1367 [30] P.Higgs. “Broken Symmetries and the Masses of Gauge Bosons”. Physical Re-  
 1368 view Letters. 13 (16): 508-509,(1964). doi:10.1103/PhysRevLett.13.508.
- 1369 [31] G.Guralnik, C.R. Hagen and T.W.B. Kibble. “Global Conservation Laws  
 1370 and Massless Particles”. Physical Review Letters. 13 (20): 585-587, (1964).  
 1371 doi:10.1103/PhysRevLett.13.585.
- 1372 [32] CMS collaboration. “Observation of a new boson at a mass of 125 GeV with  
 1373 the CMS experiment at the LHC”. Physics Letters B. 716 (1): 30-61 (2012).  
 1374 arXiv:1207.7235. doi:10.1016/j.physletb.2012.08.021
- 1375 [33] ATLAS collaboration. “Observation of a New Particle in the Search for the Stan-  
 1376 dard Model Higgs Boson with the ATLAS Detector at the LHC”. Physics Letters  
 1377 B. 716 (1): 1-29 (2012). arXiv:1207.7214. doi:10.1016/j.physletb.2012.08.020.
- 1378 [34] ATLAS collaboration; CMS collaboration (26 March 2015). “Combined Mea-  
 1379 surement of the Higgs Boson Mass in pp Collisions at  $\sqrt{s}=7$  and 8 TeV with  
 1380 the ATLAS and CMS Experiments”. Physical Review Letters. 114 (19): 191803.  
 1381 arXiv:1503.07589. doi:10.1103/PhysRevLett.114.191803.
- 1382 [35] LHC InternationalMasterclasses“When protons collide”. Retrieved from  
 1383 [http://atlas.physicsmasterclasses.org/en/zpath\\_protoncollisions.htm](http://atlas.physicsmasterclasses.org/en/zpath_protoncollisions.htm)
- 1384 [36] CMS Collaboration, “SM Higgs Branching Ratios and To-  
 1385 tal Decay Widths (up-date in CERN Report4 2016)”).

- 1386 https://twiki.cern.ch/twiki/bin/view/LHCPhysics/CERNYellowReportPageBR  
 1387 , last accessed on 17.12.2017.
- 1388 [37] R.Grant V. “Determination of Higgs branching ratios in  $H \rightarrow W^+W^- \bar{L} \bar{S} \rightarrow l^+l^- jj$  and  $H \rightarrow ZZ \rightarrow l^+l^- jj$  channels”. Physics Department, University of Tennessee (Dated: October 31, 2012). Retrieved from http://aesop.phys.utk.edu/ph611/2012/projects/Riley.pdf
- 1392 [38] LHC Higgs Cross Section Working Group, Denner, A., Heinemeyer, S. et al.  
 1393 “Standard model Higgs-boson branching ratios with uncertainties”. Eur. Phys.  
 1394 J. C (2011) 71: 1753. <https://doi.org/10.1140/epjc/s10052-011-1753-8>
- 1395 [39] F. Maltoni, K. Paul, T. Stelzer, and S. Willenbrock, “Associated production  
 1396 of Higgs and single top at hadron colliders”, Phys.Rev. D64 (2001) 094023,  
 1397 [hep-ph/0106293].
- 1398 [40] S. Biswas, E. Gabrielli, F. Margaroli, and B. Mele, “Direct constraints on the  
 1399 top-Higgs coupling from the 8 TeV LHC data,” Journal of High Energy Physics,  
 1400 vol. 07, p. 073, (2013).
- 1401 [41] M. Farina, C. Grojean, F. Maltoni, E. Salvioni, and A. Thamm, “Lifting de-  
 1402 generacies in Higgs couplings using single top production in association with a  
 1403 Higgs boson,” Journal of High Energy Physics, vol. 05, p. 022, (2013).
- 1404 [42] T.M. Tait and C.-P. Yuan, “Single top quark production as a window to physics  
 1405 beyond the standard model”, Phys. Rev. D 63 (2000) 014018 [hep-ph/0007298].
- 1406 [43] F. Demartin, F. Maltoni, K. Mawatari, and M. Zaro, “Higgs production in  
 1407 association with a single top quark at the LHC,” European Physical Journal C,  
 1408 vol. 75, p. 267, (2015).

- 1409 [44] CMS Collaboration, “Modelling of the single top-quark pro-  
 1410 duction in association with the Higgs boson at 13 TeV.”  
 1411 <https://twiki.cern.ch/twiki/bin/viewauth/CMS/SingleTopHiggsGeneration13TeV>,  
 1412 last accessed on 16.01.2018.
- 1413 [45] CMS Collaboration, “SM Higgs production cross sections at  $\sqrt{s} = 13$  TeV.”  
 1414 <https://twiki.cern.ch/twiki/bin/view/LHCPhysics/CERNYellowReportPageAt13TeV>, last  
 1415 accessed on 16.01.2018.
- 1416 [46] S. Dawson, The effective W approximation, Nucl. Phys. B 249 (1985) 42.
- 1417 [47] S. Biswas, E. Gabrielli and B. Mele, JHEP 1301 (2013) 088 [arXiv:1211.0499  
 1418 [hep-ph]].
- 1419 [48] F. Demartin, B. Maier, F. Maltoni, K. Mawatari, and M. Zaro, “tWH associated  
 1420 production at the LHC”, European Physical Journal C, vol. 77, p. 34, (2017).  
 1421 arXiv:1607.05862
- 1422 [49] LHC Higgs Cross Section Working Group, “Handbook of LHC Higgs Cross  
 1423 Sections: 4.Deciphering the Nature of the Higgs Sector”, arXiv:1610.07922.
- 1424 [50] J. Ellis, D. S. Hwang, K. Sakurai, and M. Takeuchi.“Disentangling Higgs-Top  
 1425 Couplings in Associated Production”, JHEP 1404 (2014) 004, [arXiv:1312.5736].
- 1426 [51] CMS Collaboration, V. Khachatryan et al., “Precise determination of the mass  
 1427 of the Higgs boson and tests of compatibility of its couplings with the standard  
 1428 model predictions using proton collisions at 7 and 8 TeV,” arXiv:1412.8662.
- 1429 [52] ATLAS and CMS Collaborations, “Measurements of the Higgs boson produc-  
 1430 tion and decay rates and constraints on its couplings from a combined ATLAS

- 1431 and CMS analysis of the LHC pp collision data at  $sqrts = 7$  and 8 TeV,” (2016).  
 1432 CERN-EP-2016-100, ATLAS-HIGG-2015-07, CMS-HIG-15-002.
- 1433 [53] File:Cern-accelerator-complex.svg. Wikimedia Commons,  
 1434 the free media repository. Retrieved January, 2018 from  
 1435 <https://commons.wikimedia.org/wiki/File:Cern-accelerator-complex.svg>
- 1436 [54] J.L. Caron , “Layout of the LEP tunnel including future LHC infrastructures.”,  
 1437 (Nov, 1993). A C Collection. Legacy of AC. Pictures from 1992 to 2002. Re-  
 1438 trieval from <https://cds.cern.ch/record/841542>
- 1439 [55] M. Vretenar, “The radio-frequency quadrupole”. CERN Yellow Report CERN-  
 1440 2013-001, pp.207-223 DOI:10.5170/CERN-2013-001.207. arXiv:1303.6762
- 1441 [56] L.Evans. P. Bryant (editors). “LHC Machine”. JINST 3 S08001 (2008).
- 1442 [57] CERN Photographic Service.“Radio-frequency quadrupole, RFQ-1”, March  
 1443 1983, CERN-AC-8303511. Retrieved from <https://cds.cern.ch/record/615852>.
- 1444 [58] CERN Photographic Service “Animation of CERN’s accelerator net-  
 1445 work”, 14 October 2013. DOI: 10.17181/cds.1610170 Retrieved from  
 1446 <https://videos.cern.ch/record/1610170>
- 1447 [59] C.Sutton. “Particle accelerator”.Encyclopedia Britannica. July 17, 2013. Re-  
 1448 trieval from <https://www.britannica.com/technology/particle-accelerator>.
- 1449 [60] L.Guiraud. “Installation of LHC cavity in vacuum tank.”. July 27 2000. CERN-  
 1450 AC-0007016. Retrieved from <https://cds.cern.ch/record/41567>.
- 1451 [61] J.L. Caron, “Magnetic field induced by the LHC dipole’s superconducting coils”.  
 1452 March 1998. AC Collection. Legacy of AC. Pictures from 1992 to 2002. LHC-  
 1453 PHO-1998-325. Retrieved from <https://cds.cern.ch/record/841511>

- 1454 [62] AC Team. “Diagram of an LHC dipole magnet”. June 1999. CERN-DI-9906025  
1455 retrieved from <https://cds.cern.ch/record/40524>.
- 1456 [63] CMS Collaboration “Public CMS Luminosity Information”.  
1457 <https://twiki.cern.ch/twiki/bin/view/CMSPublic/LumiPublicResults#2016>  
1458 \_proton\_proton\_13\_TeV\_collis, last accessed 24.01.2018
- 1459 [64] J.L Caron. “LHC Layout” AC Collection. Legacy of AC. Pictures  
1460 from 1992 to 2002. September 1997, LHC-PHO-1997-060. Retrieved from  
1461 <https://cds.cern.ch/record/841573>.
- 1462 [65] CMS Collaboration. “The CMS experiment at the CERN LHC” JINST 3 S08004  
1463 (2008).
- 1464 [66] CMS Collaboration. “CMS detector drawings 2012” CMS-PHO-GEN-2012-002.  
1465 Retrieved from <http://cds.cern.ch/record/1433717>.
- 1466 [67] R. Breedon. “View through the CMS detector during the cooldown of the  
1467 solenoid on February 2006. CMS Collection”, February 2006, CMS-PHO-  
1468 OREACH-2005-004, Retrieved from <https://cds.cern.ch/record/930094>.
- 1469 [68] A. Dominguez et. al. “CMS Technical Design Report for the Pixel Detector  
1470 Upgrade”, CERN-LHCC-2012-016. CMS-TDR-11.
- 1471 [69] CMS Collaboration. “Description and performance of track and primary-vertex  
1472 reconstruction with the CMS tracker,” Journal of Instrumentation, vol. 9, no.  
1473 10, p. P10009,(2014).
- 1474 [70] CMS Collaboration and M. Brice. “Images of the CMS Tracker Inner  
1475 Barrel”, November 2008, CMS-PHO-TRACKER-2008-002. Retrieved from  
1476 <https://cds.cern.ch/record/1431467>.

- 1477 [71] M. Weber. “The CMS tracker”. 6th international conference on hyperons, charm  
 1478 and beauty hadrons Chicago, June 28-July 3 2004.
- 1479 [72] CMS Collaboration. “Projected Performance of an Upgraded CMS Detector at  
 1480 the LHC and HL-LHC: Contribution to the Snowmass Process”. Jul 26, 2013.  
 1481 arXiv:1307.7135
- 1482 [73] L. Veillet. “End assembly of HB with EB rails and rotation inside SX”, January 2002. CMS-PHO-HCAL-2002-002. Retrieved from  
 1483 https://cds.cern.ch/record/42594.
- 1484
- 1485 [74] J. Puerta-Pelayo.“First DT+RPC chambers installation round in the  
 1486 UX5 cavern.”. January 2007, CMS-PHO-OREACH-2007-001. Retrieved from  
 1487 https://cds.cern.ch/record/1019185
- 1488 [75] X. Cid Vidal and R. Cid Manzano. “CMS Global Muon Trigger” web  
 1489 site: Taking a closer look at LHC. Retrieved from https://www.lhc-  
 1490 closer.es/taking\_a\_closer\_look\_at\_lhc/0.lhc\_trigger
- 1491 [76] WLCG Project Office, “Documents & Reference - Tiers - Structure,” (2014).  
 1492 http://wlcg.web.cern.ch/documents-reference , last accessed on 30.01.2018.
- 1493 [77] CMS Collaboration, “Search for the associated production of a Higgs boson  
 1494 with a single top quark in proton-proton collisions at  $\sqrt{s} = 8$  TeV”, JHEP 06  
 1495 (2016) 177,doi:10.1007/JHEP06(2016)177, arXiv:1509.08159.
- 1496 [78] B. Stieger, C. Jorda Lope et al., “Search for Associated Production of a Single  
 1497 Top Quark and a Higgs Boson in Leptonic Channels”, CMS Analysis Note CMS  
 1498 AN-14-140, 2014.

- 1499 [79] M. Peruzzi, C. Mueller, B. Stieger et al., “Search for ttH in multilepton final  
1500 states at  $\sqrt{s} = 13$  TeV”, CMS Analysis Note CMS AN-16-211, 2016.
- 1501 [80] CMS Collaboration, “Search for H to bbar in association with a single top quark  
1502 as a test of Higgs boson couplings at  $\sqrt{s} = 13$  TeV”, CMS Physics Analysis  
1503 Summary CMS-PAS-HIG-16-019, 2016.
- 1504 [81] B. Maier, “SingleTopHiggProduction13TeV”, February, 2016.  
1505 <https://twiki.cern.ch/twiki/bin/viewauth/CMS/SingleTopHiggsGeneration13TeV>.
- 1506 [82] M. Peruzzi, F. Romeo, B. Stieger et al., “Search for ttH in multilepton final1  
1507 states at  $\sqrt{s} = 13$  TeV”, CMS Analysis Note CMS AN-17-029, 2017.
- 1508 [83] B. WG, “BtagRecommendation80XReReco”, February, 2017.  
1509 <https://twiki.cern.ch/twiki/bin/view/CMS/BtagRecommendation80XReReco>.